

Article

Investigation of the Hot Deformation Behavior and Mechanism of a Medium-Entropy CoCr_{0.4}NiSi_{0.3} Alloy

Li Zhang^{1,2,*}, Hui Zhao², Lijia Chen¹, Feng Li¹, Weiqiang Zhang², Ge Zhou¹, Haoyu Zhang¹ and Ningning Geng¹

¹ School of Materials Science and Engineering, Shenyang University of Technology, Shenyang 110870, China; chenlijia@sut.edu.cn (L.C.); lifhr@sut.edu.cn (F.L.); zhouge@sut.edu.cn (G.Z.); zhanghaoyu@sut.edu.cn (H.Z.); gengningning@sut.edu.cn (N.G.)

² School of Materials Science and Engineering, Shenyang Ligong University, Shenyang 110159, China; zhaohui@sylu.edu.cn (H.Z.); zhangwq@sylu.edu.cn (W.Z.)

* Correspondence: zhangli@sylu.edu.cn

Abstract: The CoCrNi-based medium-entropy alloys (MEA) have been extensively investigated due to their exceptional mechanical properties at both room and cryogenic temperatures. To investigate the hot deformation behavior and the recrystallization mechanism of the CoCr_{0.4}NiSi_{0.3} medium-entropy alloy, a series of deformation tests was conducted using the MMS-100 thermal simulation tester, with deformation conditions of 0.001–1 s⁻¹/850–1150 °C. During the hot deformation process, the flow stress initially increases up to its peak value before gradually decreasing towards a steady state level. Higher flow stress levels are observed with increasing strain rate and decreasing deformation temperature. The estimated activation energy for hot deformation of this alloy is approximately 423.6602 kJ/mol. The Arrhenius-type constitutive equation is utilized to establish a modified model while incorporating power dissipation theory and the instability criterion of a dynamic material model to construct power dissipation maps and instability maps. By superimposing these maps, hot processing maps with strains of 0.4, 0.5, and 0.7 are derived. In this investigation, it is observed that regions of instability exclusively occur when the true strain exceeds 0.4. These regions of instability on the hot processing map align well with experimental findings. The suitable range of parameters for hot-working decreases as the true strain increases. The microstructure was analyzed using electron backscatter diffraction and transmission electron microscopy (TEM) techniques. The volume fraction of dynamic recrystallization (DRX) decreases with increasing strain rate but diminishes with rising temperature. The TEM characterization elucidated the mechanism of DRX in this MEA. The presence of the long-period stacking ordered (LPSO) phase was observed in both the face-centered cubic matrix and hexagonal close-packed recrystallized grains under different deformation conditions. The LPSO phase originates from the matrix at a low strain rate, whereas it is generated during recrystallization at a high strain rate. The observed increase in flow stress of the as-cast MEA is primarily attributed to the synergistic effects arising from the interaction of the dislocation with twins and the second phase. The onset of instability is effectively suppressed within a limited range through the formation of coherent second phases such as L1₂, LPSO, and superlattice structures resulting from phase transitions. These second phases serve as nucleation sites for recrystallization and contribute to the strengthening of dispersion. Furthermore, their interaction with dislocations and twins significantly influences both flow stress behavior and recrystallization kinetics under hot deformation. These findings not only deepen our understanding of the underlying deformation mechanisms governing MEA but also offer valuable insights for designing CoCrNi-based alloys with improved mechanical properties at elevated temperatures.



Citation: Zhang, L.; Zhao, H.; Chen, L.; Li, F.; Zhang, W.; Zhou, G.; Zhang, H.; Geng, N. Investigation of the Hot Deformation Behavior and Mechanism of a Medium-Entropy CoCr_{0.4}NiSi_{0.3} Alloy. *Crystals* **2024**, *14*, 3. <https://doi.org/10.3390/cryst14010003>

Academic Editors: Ali Arab, Baoqiao Guo, Bin Jia, Rusinek Alexis and Benilde F.O. Costa

Received: 26 November 2023

Revised: 11 December 2023

Accepted: 17 December 2023

Published: 19 December 2023



Copyright: © 2023 by the authors. Licensee MDPI, Basel, Switzerland. This article is an open access article distributed under the terms and conditions of the Creative Commons Attribution (CC BY) license (<https://creativecommons.org/licenses/by/4.0/>).

Keywords: hot deformation; medium-entropy alloy; constitutive equation; hot processing map; super lattice; LPSO

1. Introduction

High- and medium-entropy alloys, initially proposed in 2004 [1,2], have emerged as a prominent design paradigm in materials science, offering novel avenues and concepts for the advancement of state-of-the-art metallic materials with exceptional performance characteristics. Consequently, extensive investigations have been conducted by scholars across diverse alloy systems [3–9]. In recent times, the application scenarios for key equipment-related materials have witnessed a surge in diversity, thereby necessitating broader mechanical property requirements for these materials. Therefore, the transition elements (i.e., Cr, Mn, Fe, Co, Ni, and Cu) exhibit exceptional mechanical properties due to the partial occupancy of d orbitals by electrons and are frequently selected as the primary constituents for forming high-entropy alloys. The researchers have been actively involved in the design and optimization of alloy mechanical properties, employing diverse forms of simulation-based design [10–13] and rigorous mechanical testing [14] across a range of temperatures. Additionally, diverse processing technologies and mechanisms are being researched based on the accumulated theory and experience in traditional metals and alloys. These efforts aim to facilitate technological breakthroughs in extreme application environments, such as wide temperature ranges and complex stress conditions [15,16] for alloys, ultimately enabling scientific material design that provides crucial support for high-tech applications. The Cantor alloy, consisting of five principal elements, has been extensively investigated as a high-entropy alloy (HEA) due to its exceptional strength and plasticity [17–19]. Meanwhile, the CoCrNi-based medium-entropy alloy (MEA) has garnered significant attention owing to its superior mechanical properties, leading to further advancements in this alloy system [20,21].

The CoCrNi-based medium entropy alloy has shown exceptional strength and plasticity at both room and cryogenic temperatures [21–24]. The incorporation of Si components in CoCrNi-based MEA leads to a reduction in the stacking fault energy (SFE) and an increase in lattice distortion, thereby augmenting its mechanical properties at room temperature [25]. Dharmendra et al. [26] incorporated 0.2–0.8 Si (wt.%) into the hexagonal close-packed (HCP) structured TX32–0.4Al alloy to investigate the hot working capabilities and found that the initial instability region characterized by low temperatures and high strain rates in TX32–0.4Al alloy is significantly diminished to eliminate with elevated Si addition at 0.4–0.8 (wt.%) in the hot processing map. Furthermore, the introduction of 0.4 wt.% Si enhances the performance of hot working by mitigating flow instability and widening the hot processing window. However, despite some existing research on the hot deformation behavior of CoCrNi-based alloys [27–30], a more comprehensive and precise understanding of the underlying mechanisms governing microstructure evolution during deformation is still needed. In the CoCrNi-based alloys with face-centered cubic (FCC) as the predominant phase structure, investigating the impact of Si addition on the hot processing properties and recrystallization mechanism of this material holds significant importance in engineering and military domains.

The hot deformation process of metals and alloys is a thermally activated process [31] characterized by intense atomic movement, which is closely associated with the hot deformation conditions of the material. The flow stress is primarily influenced by the factors of deformation temperature, strain rate, and deformation extent [32]. During hot deformation, the FCC phase, which is the predominant phase in these alloys, exhibits varying levels of flow stress [28–30]. Further summarization is necessary to comprehend the stability and phase transition of the high-temperature phase. $L1_2$ acts as a prevalent coherent second-phase within Ni-based superalloys [32] or emerging MEAs/HEAs generally containing Al and Ti [33,34], effectively enhancing the mechanical properties of alloys at elevated temperatures. The long-period stacking order (LPSO) phase was initially observed in Au-Mn alloys [35] and is commonly observed in HCP phases, particularly in rare earth Mg alloys, exhibiting varying degrees of strengthening and toughening effects [36–38]. Wang et al. [39] conducted a first-principles investigation on solute atoms in Al alloys, revealing that Si atoms exhibit a preference for segregation to the SF planes of 9R, 12R, 15R,

and 18R phases due to distinct alterations in their stacking sequences within (111) close-packed planes. Furthermore, the inclusion of the LPSO phase substantially contributes to the augmentation of mechanical properties in Al alloys. In the process of tensile plastic deformation of TiAl intermetallics, the lamellar structure of LPSO plays a crucial role in enhancing high-temperature mechanical performance by promoting glide motion of 1/6 Shockley partial dislocations on the (111) close-packed lattice plane, thereby facilitating plastic deformation, particularly through the formation of 6H and 9R structures [40]. The investigation of high-temperature phases and strengthening mechanisms in HEAs and MEAs has garnered significant interest due to their unique properties. The comprehension of the hot deformation mechanism of an alloy is essential for the development of hot working technology, necessitating a thorough investigation into the hot deformation characteristics of MEA under various conditions to optimize alloy properties.

This study investigates the influence of strain rate and deformation temperature on flow stress and microstructural alterations during hot compression testing of $\text{CoCr}_{0.4}\text{NiSi}_{0.3}$ MEA. A modified model based on the Arrhenius-type constitutive equation is established for this particular MEA, accompanied by hot working maps for various true strains, facilitating analysis of dynamic recrystallization (DRX) behavior during the process. The microstructure and underlying DRX mechanism under different conditions are thoroughly discussed, providing a theoretical foundation for determining production process parameters.

2. Experimental

The MEA ingot of $\text{CoCr}_{0.4}\text{NiSi}_{0.3}$ (at.%) weighing 5 kg was produced through induction melting, utilizing raw materials comprising Co, Cr, Ni, and Si with a minimum purity of 99.9 wt.%. The bulk ingot was successively melted four times at power levels of 100, 120, 140, and 120 kW and a temperature of 1700 °C to ensure a homogeneous composition. Subsequently, the ingot was cast into a 16 mm thick slab under an argon atmosphere and rapidly cooled in the furnace within 30 min. The cylindrical as-cast testing samples with dimensions of $\Phi 8 \times 15$ mm were then directly obtained from the MEA slab through wire-electrode cutting in a direction perpendicular to its thickness and subsequently subjected to mechanical polishing. The MMS-100 thermal simulation tester was employed to conduct an isothermal hot compression test under ambient conditions with a compression reduction of 8 mm. The temperature was continuously controlled by an integrated system. The hot compression was conducted with a heating rate of 10 °C and held for 3 min prior to compression in order to maintain a uniform heating temperature. The specimens were compressed at strain rates of 0.001, 0.01, 0.1, and 1 s⁻¹ at temperatures of 850, 950, 1050, and 1150 °C, respectively. Subsequently, the specimens were rapidly water-quenched to minimize the impact of static recrystallization. The schematic diagram of the compression process is depicted in Figure 1a. Figure 1b shows the schematic diagram of the deformation areas of a compressed specimen. The large deformation zones (LDZ) [41] of the axial sections of hot compressed specimens were selected for observation and analysis of the microstructures. A comprehensive understanding of the hot compression behavior of the MEA was achieved by establishing a constitutive equation. X-ray diffraction (XRD), Electron backscatter diffraction (EBSD), and transmission electron microscopy (TEM) samples were prepared via a symmetrical midline incision along the compression direction. Vibration polishing techniques were employed for preparing the EBSD samples. The microstructures and composition of the MEA were characterized after hot deformation using the Thermo Fisher Apreo 2C field emission scanning electron microscopy (FE-SEM) equipped with a Symmetry S2 probe. The step size ranged from 0.12 to 0.5 μm, accounting for variations in grain size within the uniform deformation zone of each sample. TEM characterizations were conducted using the FEI Talos F200X microscope after ion milling of the TEM samples with Gatan695.

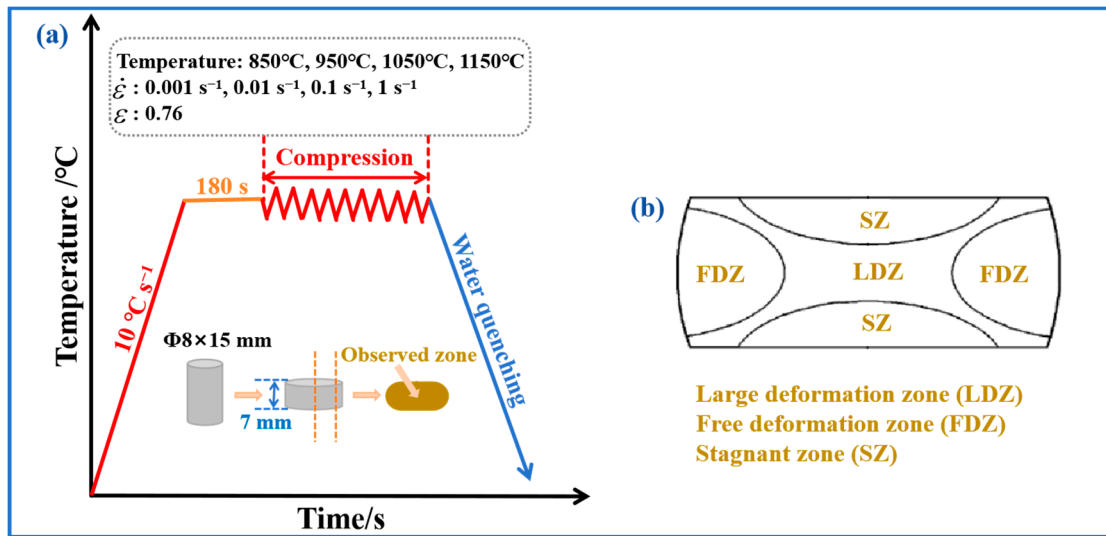


Figure 1. (a) Schematic diagram of the hot compression process; (b) Schematic diagram of deformation areas of a compressed specimen.

3. Results and Discussion

3.1. True Stress-Strain Curves of the MEA

The true stress-strain behavior of the MEA during hot compression tests, conducted at strain rates of 0.001, 0.01, 0.1, and 1 s⁻¹, with testing temperatures of 850 °C, 950 °C, 1050 °C, and 1150 °C, is illustrated in Figure 2. During the initial stage of deformation, the flow stress exhibits a rapid increase attributed to lattice distortion and pronounced work hardening induced by dislocation proliferation and entanglement that further impede dislocation motion during deformation. The peak stress and corresponding true strain exhibit a decreasing trend as the deformation temperature increases at the given strain rate. The flow stress curves exhibit a significant decrease and demonstrate distinct characteristics of DRX after attaining the peak stress at 850 °C under varying strain rates. The flow stress exhibits significant oscillations during hot compression under a strain rate of 0.001 s⁻¹, as depicted in Figure 2a, indicating the occurrence of deformation twins that facilitate the deformation or discontinuous DRX (DDRX) at a low strain rate due to the low SFE [42,43]. The distinctive characteristics of dynamic recovery (DRV) can be observed at high strain rates when it undergoes deformation at various strain rates at 950 °C, as depicted in Figure 2c,d. Conversely, the flow stress initially exhibits a peak and subsequently decreases with increasing true strain when subjected to lower strain rates, indicating the occurrence of DRX, as illustrated in Figure 2a,b. The MEA demonstrates similar rheological behavior when subjected to different strain rates at temperatures of 1050 °C and 1150 °C, particularly at the higher strain rate as illustrated in Figure 2c,d. During the initial stage of deformation, the rheological stress reaches its peak. A slight yet discernible decline in stress is observed on the post-peak stress curve while maintaining consistent flow stress with an increasing strain rate. A dynamic equilibrium exists between work hardening and DRX softening. The flow stress initially decreases to 0 MPa at a true strain of 0.55 and a hot deformation condition of 0.01 s⁻¹/1150 °C, followed by an increasing trend with higher levels of true strain as illustrated in Figure 2b, demonstrating the characteristic behavior of DDRX under high temperature and low strain rate. The peak flow stress (σ_p) under various deformation conditions is presented in Table 1.

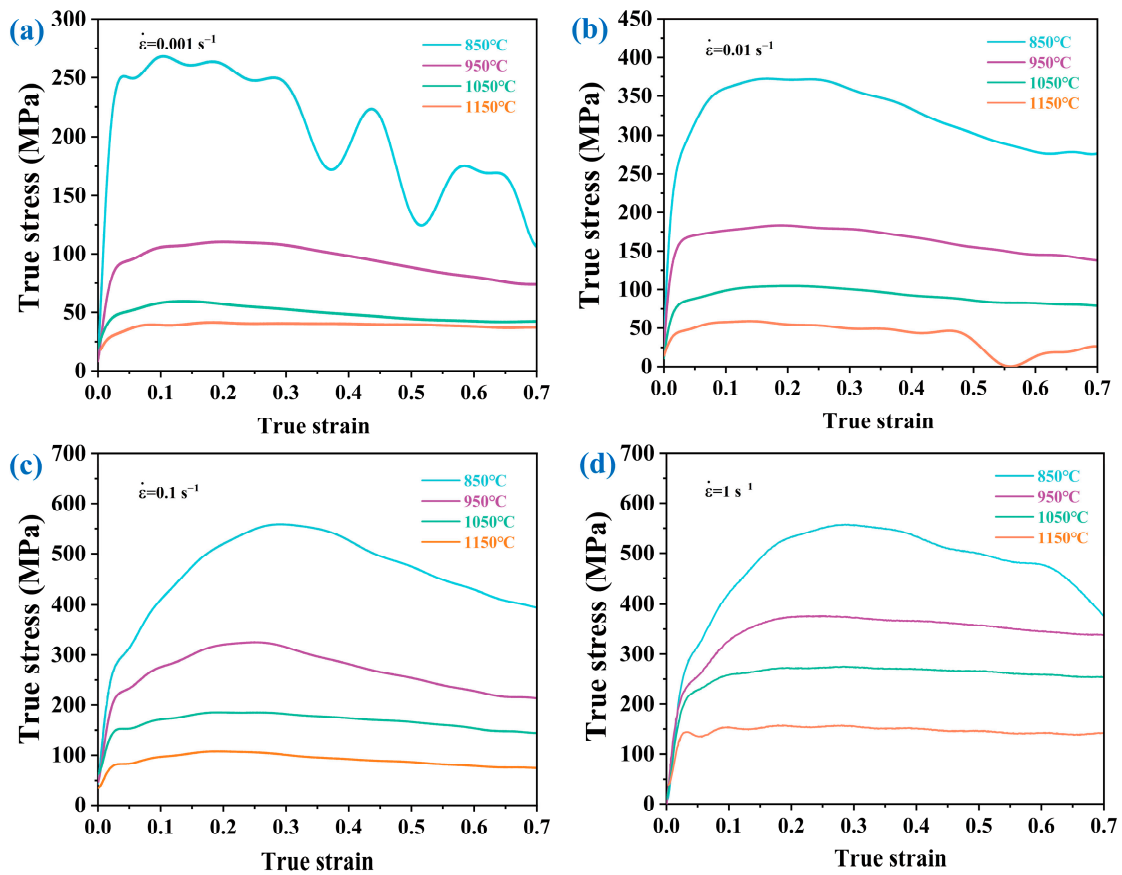


Figure 2. True stress-strain curves of the $\text{CoCr}_{0.4}\text{NiSi}_{0.3}$ alloy at different deformation conditions. (a) 0.001 s^{-1} ; (b) 0.01 s^{-1} ; (c) 0.1 s^{-1} ; (d) 1 s^{-1} .

Table 1. σ_p at different deformation conditions.

$T/^\circ\text{C}$	$\dot{\epsilon}$			
	0.001 s^{-1}	0.01 s^{-1}	0.1 s^{-1}	1 s^{-1}
850	268.6	372.8	559.3	557.6
950	110.8	183.9	325.7	376.4
1050	60.1	105.1	186.0	275.1
1150	42.0	59.6	108.0	157.3

3.2. The Activation Energy and Constitutive Equation

The hot deformation process of the MEA is a thermally activated process that is governed by the kinetics of dislocation motion. The variation of flow stress partially reflects the evolution of microstructure during hot deformation. It is evident that the deformation temperatures and strain rates have a significant influence on the true stress-strain behavior of MEA, as depicted in Figure 2. In order to analyze the hot deformation behaviors of metallic materials, researchers widely employ the Arrhenius-type equation model to describe the relationship between deformation conditions and flow stress [44].

Sellars and Tegart [45] proposed a hyperbolic sine correlation for hot deformation for all flow stress levels in hot deformation. Therefore, based on the deformation conditions during the hot deformation process of the MEA, the functional relation is established as follows:

$$\dot{\epsilon} = A [\sinh(\alpha\sigma)]^n \exp\left(-\frac{Q}{RT}\right) \quad (\text{for all } \sigma, \text{ exponential relationship relationship}) \quad (1)$$

Equations (2) and (3) can be obtained by different transformations of Equation (1) as:

$$\dot{\epsilon} = A_1 \sigma^{n_1} \exp\left(-\frac{Q}{RT}\right) \quad (\alpha\sigma < 0.8, \text{ low stresses in power relationship}) \quad (2)$$

$$\dot{\epsilon} = A_2 \exp(\beta\sigma) \exp\left(-\frac{Q}{RT}\right) \quad (\alpha\sigma \geq 1.2, \text{ high stresses in exponential relationship}) \quad (3)$$

where $\dot{\epsilon}$ is strain rate (s^{-1}); σ is flow stress (MPa); A , A_1 , A_2 , α , and β are constants independent of temperature; n and n_1 are stress indices of the materials; $\alpha = \beta/n_1$; Q is the activation energy ($\text{kJ}\cdot\text{mol}^{-1}$); R is the molar gas constant ($8.314 \text{ J}\cdot\text{mol}^{-1}\cdot\text{K}^{-1}$); T is the absolute temperature of deformation (K).

Assuming that the activation energy is temperature-independent, by applying the natural logarithmic transformation to both sides of Equations (1)–(3), the equations can be correspondingly expressed as follows:

$$\ln[\sinh(\alpha\sigma)] = \frac{\ln \dot{\epsilon}}{n} + \frac{Q}{nRT} - \frac{\ln A}{n} \quad (4)$$

$$\ln \dot{\epsilon} = \ln A_1 + n_1 \ln \sigma - \frac{Q}{RT} \quad (5)$$

$$\ln \dot{\epsilon} = \ln A_2 + \beta\sigma - \frac{Q}{RT} \quad (6)$$

If the relationship of $\ln \dot{\epsilon} - \ln \sigma$ and $\ln \dot{\epsilon} - \sigma$ described in Equations (5) and (6) are linear, the slopes are n_1 and β , respectively. Table 1 presents the σ_p at various strain rates and temperatures. Figure 3a,b illustrate the fitting lines of $\ln \dot{\epsilon} - \ln \sigma_p$ and $\ln \dot{\epsilon} - \sigma_p$ from which n_1 and β are determined as 5.633 and 0.033, respectively. Therefore, the value of α , calculated as $\alpha = \beta/n_1$, is determined to be 0.0059 MPa^{-1} .

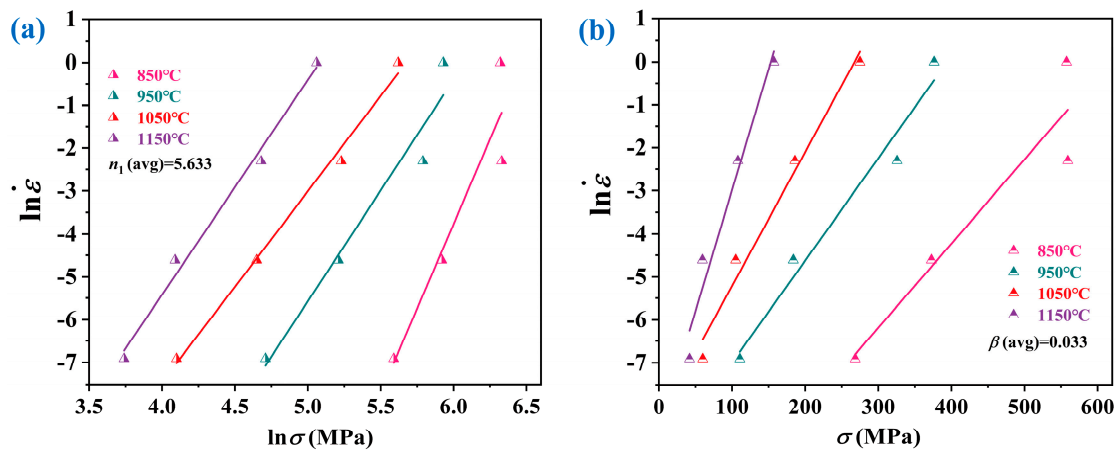


Figure 3. The relationship between strain rates and flow stress: (a) $\ln \dot{\epsilon} - \ln \sigma$; (b) $\ln \dot{\epsilon} - \sigma$.

According to Equation (4), if there is a linear relationship between $\ln[\sinh(\alpha\sigma)]$ and $\ln \dot{\epsilon}$, then the slope is n^{-1} , consequently, the stress indices of n can be determined. Similarly, if there is a linear relationship between $\ln[\sinh(\alpha\sigma)]$ and T^{-1} , then the slope value represents Q/nR and the activation energy Q can be expressed as:

$$Q = R \left[\frac{\partial \ln \dot{\epsilon}}{\partial \ln[\sinh(\alpha\sigma)]} \right] \bigg|_T \left[\frac{\partial \ln[\sinh(\alpha\sigma)]}{\partial T^{-1}} \right] \bigg|_{\dot{\epsilon}} \quad (7)$$

Figure 4a,b illustrate the linear relationship of the fitting lines of $\ln[\sinh(\alpha\sigma)] - \ln \dot{\epsilon}$, and $\ln[\sinh(\alpha\sigma)] - T^{-1} / \times 10^{-3} \text{ K}^{-1}$, respectively, and the value of n and Q/nR can be derived from the average slopes as 3.7908 and 13.4424 correspondingly. The activation energy (Q)

of the MEA at high-temperature deformation can be obtained by bringing the derived average slopes of Figure 4a,b to Equation (7), and the value is found to be 423.6602 kJ/mol. The relatively high value of Q indicates comparatively slower DRX kinetics in this MEA compared with conventional alloy systems [46,47]. The obtained value Q can be attributed to the low SFE and robust work-hardening ability exhibited in the MEA.

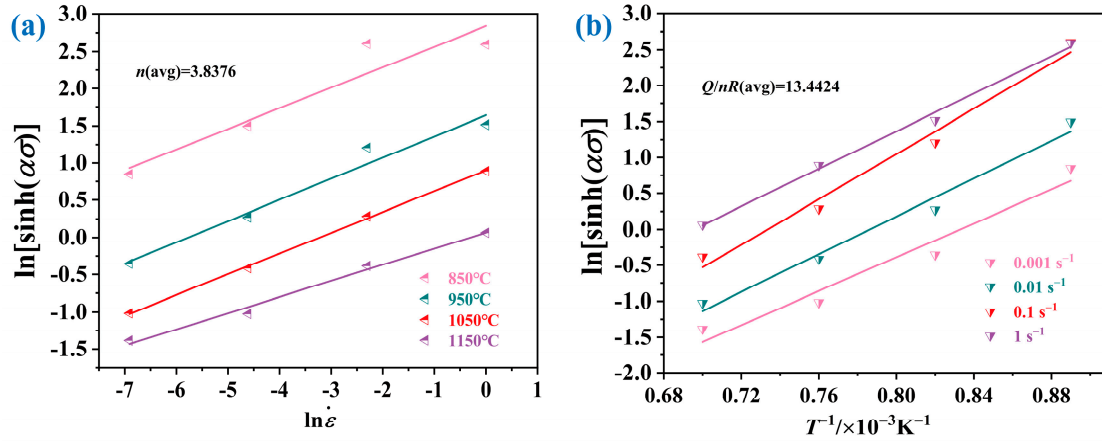


Figure 4. The relationships of (a) $\ln[\sinh(\alpha\sigma)] - \ln\dot{\epsilon}$; (b) $\ln[\sinh(\alpha\sigma)] - \ln\dot{\epsilon}$.

The literatures [44,48] have demonstrated that the true stress-strain constitutive relation is significantly influenced by deformation conditions. By determining the activation energy (Q) of the MEA, a temperature-compensated strain rate factor is introduced to account for this effect. The correlation between temperature and strain rate in various processing procedures of metallic materials can be expressed by the Zener-Hollomon (Z) parameter [49]:

$$Z = \dot{\epsilon} \exp\left(\frac{Q}{RT}\right) \quad (8)$$

The value of Z under different deformation conditions can be determined by applying the natural logarithm to both sides of Equation (8), as indicated in Equation (9):

$$\ln Z = \ln \dot{\epsilon} + \frac{Q}{RT} \quad (9)$$

The Equation (4) can be transformed as:

$$n \ln[\sinh(\alpha\sigma)] = \ln \dot{\epsilon} + \frac{Q}{RT} - \ln A \quad (10)$$

The combination of Equations (9) and (10) can be expressed as follows:

$$\ln Z = n \ln[\sinh(\alpha\sigma)] + \ln A \quad (11)$$

If the relationship between $\ln Z$ and $\ln[\sinh(\alpha\sigma)]$ described in Equation (11) exhibits linearity, the slope corresponds to n , while the intercept corresponds to $\ln A$. The Z values were derived by substituting the σ_p obtained under various deformation conditions into Equation (11). Through the utilization of linear regression analysis, as illustrated in Figure 5, the value of $\ln A$ was determined to be 35.2345. This resulted in an A value of $2.0052 \times 10^{15} \text{ MPa}^{-1}$, and n was determined to be 3.6754, which closely matches the fitting result shown in Figure 4a. The range of $\alpha\sigma_p$ values in this study spans from 0.25 to 3.30. To characterize the model for this MEA at a true strain of 0.76, we employ the Arrhenius-type hyperbolic sine formula described in Equation (2), which is presented as Equation (12):

$$\dot{\epsilon} = 2.0052 \times 10^{15} [\sinh(0.0059\sigma)]^{3.8376} \exp\left(-\frac{423660.2}{RT}\right) \quad (12)$$

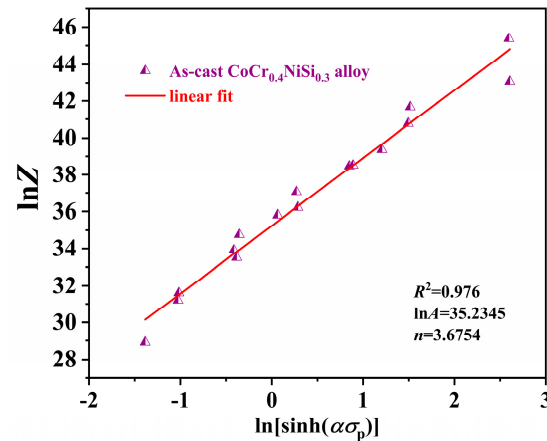


Figure 5. The plots of $\ln Z - \ln[\sinh(\alpha\sigma_p)]$ of $\text{CoCr}_{0.4}\text{NiSi}_{0.3}$ alloy at various temperatures.

3.3. Hot Processing Maps

The establishment of hot processing maps is a method employed to accurately analyze the behavior of metals and alloys during hot deformation, enabling a comprehensive understanding of microstructural evolution in response to changes in deformation parameters, by which desirable changes in the microstructure and properties are obtained. Raj [50] first proposed and established a theory and method of dynamic material model (DMM) that correlated external total input power (P) during hot deformation with energy consumption throughout this process. The hot processing map includes a power dissipation map that overlays with a rheological instability map, facilitating the identification of metallurgical materials under plastic processing. Prasad et al. [51,52] facilitated the optimization of alloy processing parameters using a modeling method. This comprehensive approach encompassed both power dissipation (G) through energy resulting from plastic deformation and dissipated power coefficient (J) arising from the evolution of microstructure and is expressed as follows:

$$P = \sigma \dot{\epsilon} = \int_0^{\dot{\epsilon}} \sigma d\dot{\epsilon} + \int_0^{\sigma} \dot{\epsilon} d\sigma = G + J \quad (13)$$

where G represents the dissipated energy during the deformation process; J denotes the energy of microstructural evolution resulting from DRX and DRV in this process. Under any given strain rate ($\dot{\epsilon}$), and temperature (T), the changes of J with respect to G can be characterized by the strain rate sensitivity parameter m , which is interpreted using a DMM as:

$$m = \frac{dJ}{dG} = \left[\frac{\partial(\ln \sigma)}{\partial(\ln \dot{\epsilon})} \right]_{\epsilon, T} \quad (14)$$

m is always strain rate and temperature independent for pure metals under hot processing while varying from 0 to 1 in complicated alloys. According to Equation (14), m reaches its maximum value of 1 in the case of an ideal linear dissipation of workpiece hot processing. This indicates that J can also reach its maximum value of J_{\max} when $m = 1$. Therefore, the J_{\max} can be depicted as $J_{\max} = \sigma \dot{\epsilon} / 2$. The efficiency of power dissipation parameter η [52] is utilized to evaluate the microstructural evolution in terms of power dissipation and can be expressed as:

$$\eta = \frac{J}{J_{\max}} = \frac{P - G}{J_{\max}} = 2 - \frac{G}{J_{\max}} \quad (15)$$

It is apparent from Equation (15) that the value of η is highly correlated with the parameter G , which is expressed as: $G = \int_0^{\dot{\epsilon}} \sigma d\dot{\epsilon}$. Moreover, Prasad et al. [51] supposed that

m is independent of $\dot{\epsilon}$ at specific temperatures, and the flow stress curve follows the power law by the Equation:

$$\sigma = K\dot{\epsilon}^m \quad (16)$$

where K and m are materials constant. From Equation (16), the parameter G follows that:

$$G = \int_0^{\dot{\epsilon}} \sigma d\dot{\epsilon} = \int_0^{\dot{\epsilon}} K\dot{\epsilon}^m d\dot{\epsilon} = \frac{K\dot{\epsilon}^{m+1}}{m+1} = \frac{\sigma\dot{\epsilon}}{m+1} \quad (17)$$

when substituting Equation (17) into Equation (15), the efficiency of power dissipation parameter η is obtained in terms of m as:

$$\eta = \frac{P - G}{J} = \frac{2m}{m+1} \quad (18)$$

The parameter η represents the dissipating ability of a specific workpiece with respect to the total input power. The dissipated power coefficient J in multi-phase alloys and complex microstructures is always influenced by the simultaneous or interactive effects of metallurgical processes such as DRX, DRV, particle and phase dissolution or growth, as well as deformation-induced phase transitions or precipitations under dynamic processing conditions. In order to characterize the dissipative process affected by multiple factors to obtain the favorable hot processing conditions of the highest J dissipated in the most efficient processing method with the highest η , Prasad [53,54] defined the dimensionless parameter (ζ) as the instability criterion. It is a crucial parameter in the construction of the hot processing map and plays a crucial role in determining the plastic instability of alloys. The Prasad criterion is utilized to determine the instability of the CoCr_{0.4}NiSi_{0.3} alloy and expressed as:

$$\zeta = \frac{\partial \ln(\frac{m}{m+1})}{\partial \ln \dot{\epsilon}} + m < 0 \quad (19)$$

The instability region is identified by the criterion of Equation (19) with $\zeta < 0$, while the remaining region is designated as the safe region for hot processing. A higher absolute value of ζ indicates a greater likelihood of material instability under these processing conditions. Consequently, the criterion can serve as a valuable reference for selecting optimal deformation process parameters.

Figure 6a–c depicts the hot processing map of the MEA at true strains of 0.4, 0.5, and 0.7, respectively. The contour lines depict the parameter η , which signifies the proportion of energy consumed by microstructural evolution and acts as a driving force for nucleation and growth of DRX. The numerical value of η increases as the true strain rises. The gray regions in Figure 6a–c represent instability and are characterized by low values of η , which is unsuitable for hot processing. Figure 6a,b illustrates the hot processing maps when true strains are 0.4 and 0.5, the instability regions appear at 850–860 °C, and the corresponding strain rates are 0.264–0.428 s^{−1} and 0.220–0.483 s^{−1}, respectively. However, there is minimal variation in hot processing parameters at true strains of 0.4 and 0.5. When the true strain is 0.7, the temperature range of the instability region expands to 850–890 °C while maintaining a strain rate range of 0.116–0.675 s^{−1}. This trend corresponds to the true stress-strain curve of the MEA. The true stress-strain curves of the MEA exhibit a significant decrease in flow stress after reaching its peak stress within a temperature range of 850 °C–950 °C, demonstrating varying degrees of instability. The suitable range of parameters for hot-working decreases as the true strain increases, which is worth noting. The hot processing maps in Figure 6a–c reveal that the MEA exhibits stability at high strain rates, except for larger strains where a small instability zone occurs under these specific processing parameters. This can be attributed to the addition of the Si component. Similar instabilities during high strain rates of hot deformation are also observed in the hot processing maps of HCP structured TX32–0.4Al alloy with Si additions ranging from

0.4–0.8 (wt.%). Therefore, the inclusion of Si can effectively enhance the hot processing performance of the $\text{CoCr}_{0.4}\text{NiSi}_{0.3}$ alloy. Figure 6d shows the workpieces hot processed at different parameters. The smooth, round cake-shape indicates the good forming ability in the tested hot processing parameters. The instability defects occur at the deformation conditions of 850 °C with a strain rate range of 0.1–1 s^{-1} , as well as at 950 °C with a strain rate of 0.1 s^{-1} . Ultimately, the regions of instability in the hot processing map align consistently with the experimental findings.

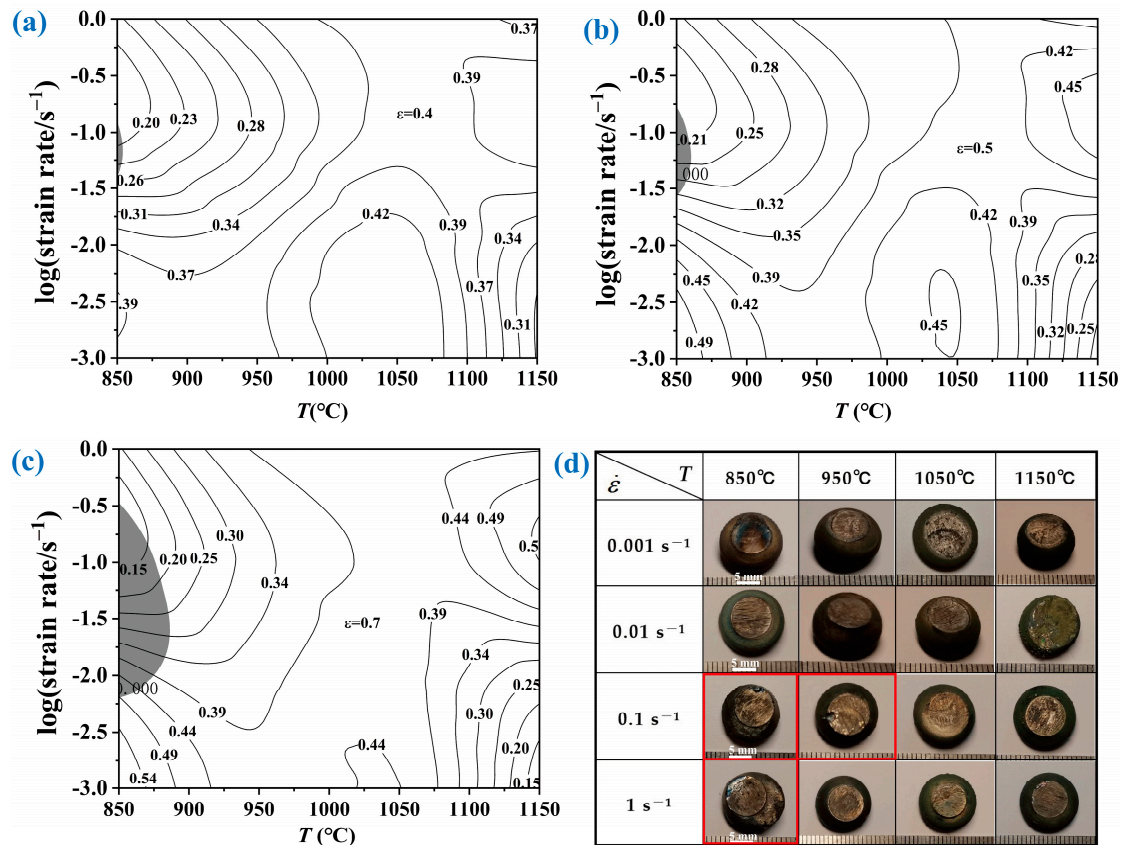


Figure 6. Hot processing maps of the $\text{CoCr}_{0.4}\text{NiSi}_{0.3}$ alloy at (a) $\epsilon = 0.4$; (b) $\epsilon = 0.5$; (c) $\epsilon = 0.7$; (d) Macroscopic morphologies of hot deformed $\text{CoCr}_{0.4}\text{NiSi}_{0.3}$ alloy at different processing parameters.

3.4. Microstructure Analysis of the $\text{CoCr}_{0.4}\text{NiSi}_{0.3}$ Alloy

The influence of deformation temperature and strain rate on the behavior and growth of DRX during hot compression of the MEA was investigated using EBSD analysis technology. The volume fraction of DRX and average grain diameter were calculated and analyzed under various deformation conditions, as depicted in Figures 7–9. The phase composition of the initial state (as-cast $\text{CoCr}_{0.4}\text{NiSi}_{0.3}$ alloy) of the specimens prior to hot deformation was confirmed to consist of an FCC matrix with a minor presence of lamellar $\text{Ni}_{31}\text{Si}_{12}$ and Ni_2Si eutectic structures at subgrain boundaries, as characterized by XRD and TEM [55].

Figure 7a,b depicts the changes in grain morphology at strain rates of 1 s^{-1} and 0.001 s^{-1} , respectively, at a temperature of 850 °C. Figure 7c,d illustrates the grain boundary volume fraction and distribution of $\Sigma 3$ in regions A and B shown in Figure 7a,b, respectively. Figure 7e presents the contrast between the volume fraction of recrystallized, substructured, and deformed grains at strain rates of 1 s^{-1} and 0.001 s^{-1} at a temperature of 850 °C. Figure 7f demonstrates the changes in average grain diameter (by equivalent circular diameter) at strain rates of 1 s^{-1} and 0.001 s^{-1} at a temperature of 850 °C. The as-cast average grain diameter of the MEA measures 19.73 μm [55]. Upon hot deformation at 850 °C/1 s^{-1} , a significant number of fine necklace-like dynamically recrystallized (DRXed)

grains form along the grain boundaries. The average grain diameter is measured to be $2.8 \mu\text{m}$, with the volume fraction of twins accounting for 37.3%. The fraction of DRXed grains is determined to be 56.36%, while the substructured volume fraction accounts for 6.23%. Notably, no $\Sigma 3$ grain boundaries are observed within the recrystallized grains, indicating an absence of twinning in DRX. When subjected to hot deformation conditions at $850 \text{ }^\circ\text{C}/0.001 \text{ s}^{-1}$, the grains undergo further growth, resulting in an average grain diameter of $3.2 \mu\text{m}$. Simultaneously, the volume fraction of deformation twins increases to 46.0%, accompanied by a decrease in the DRX volume fraction to 46.10% and an increase in the substructured volume fraction to 40.63%. The presence of deformation twins is clearly observed in the recrystallized grains under a lower strain rate of 0.001 s^{-1} , as depicted in Figure 7d. These twins actively play a crucial role in mediating the hot deformation process. It is evident that at a temperature of $850 \text{ }^\circ\text{C}$ during hot deformation, the average grain diameter, volume fraction of twins, and substructure all demonstrate an increasing trend as the strain rate decreases. Conversely, the volume fraction of DRX exhibits a decrease with decreasing strain rate. The findings suggest that an increased volume of deformation twins is formed, facilitating hot deformation and initiating a multi-slip system at lower strain rates. Consequently, flow stress is mitigated, and the nucleation potential for recrystallization is diminished.

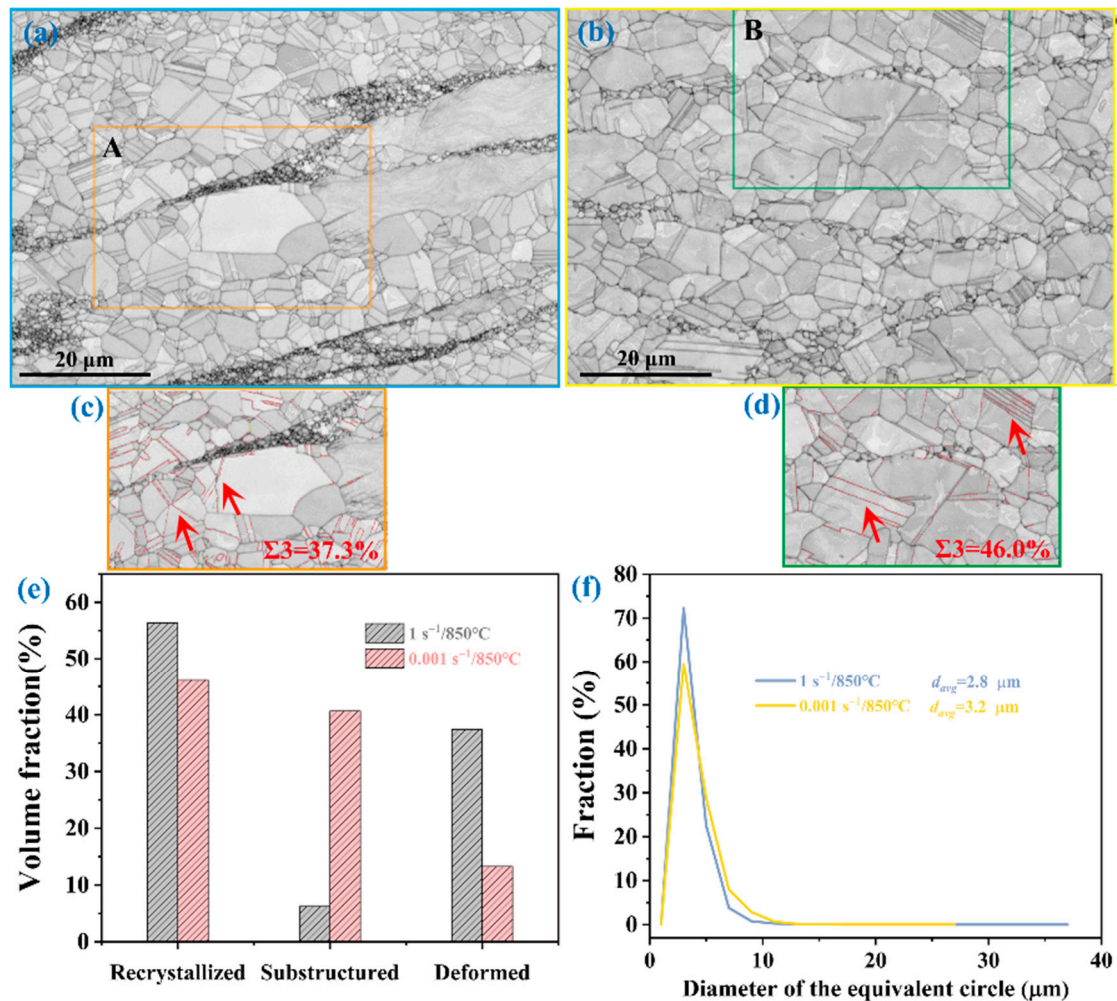


Figure 7. Band contrast image at deformation conditions of (a) $1 \text{ s}^{-1}/850 \text{ }^\circ\text{C}$ and (b) $0.001 \text{ s}^{-1}/850 \text{ }^\circ\text{C}$; Band contrast images overlaid with $\Sigma 3$ grain boundaries corresponding to (c) area A in Figure 7a, and (d) area B in Figure 7b; (e) Contrast between volume fraction of recrystallized, substructured, and deformed grains at deformation conditions of $1 \text{ s}^{-1}/850 \text{ }^\circ\text{C}$, and $0.001 \text{ s}^{-1}/850 \text{ }^\circ\text{C}$; (f) Average grain diameter at deformation conditions of $1 \text{ s}^{-1}/850 \text{ }^\circ\text{C}$, and $0.001 \text{ s}^{-1}/850 \text{ }^\circ\text{C}$.

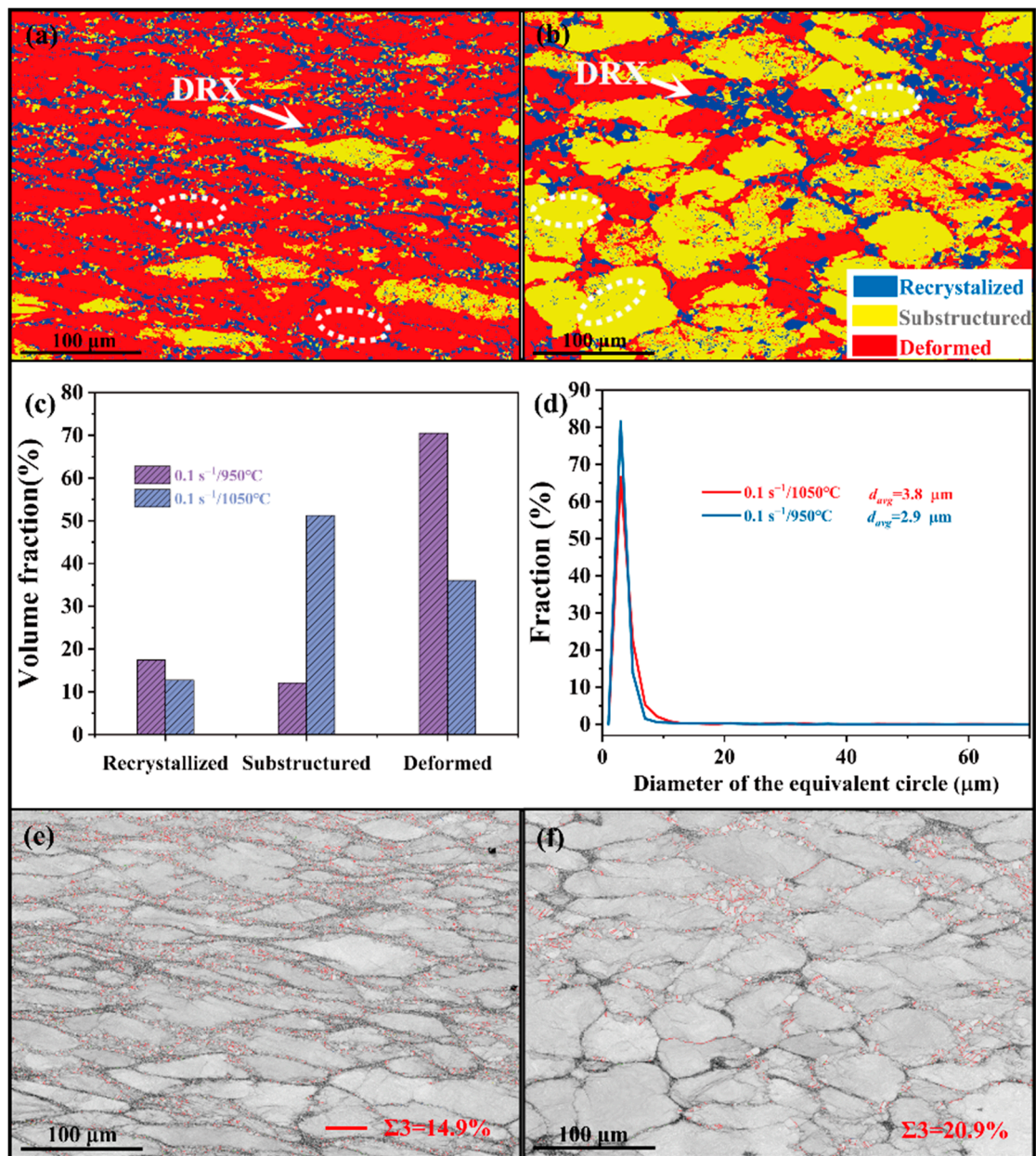


Figure 8. (a) The distribution of recrystallized, substructured, and deformed grains at deformation conditions of $0.1 \text{ s}^{-1}/950 \text{ }^{\circ}\text{C}$ and (b) $0.1 \text{ s}^{-1}/1050 \text{ }^{\circ}\text{C}$; (c) Contrast between volume fraction of recrystallized, substructured, and deformed grains at deformation conditions of $0.1 \text{ s}^{-1}/950 \text{ }^{\circ}\text{C}$ and $0.1 \text{ s}^{-1}/1050 \text{ }^{\circ}\text{C}$; (d) Average grain diameter at deformation conditions of $0.1 \text{ s}^{-1}/950 \text{ }^{\circ}\text{C}$ and $0.1 \text{ s}^{-1}/1050 \text{ }^{\circ}\text{C}$; Band contrast images overlaid with $\Sigma 3$ grain boundaries corresponding to the area of (e) Figure 8a and (f) Figure 8b.

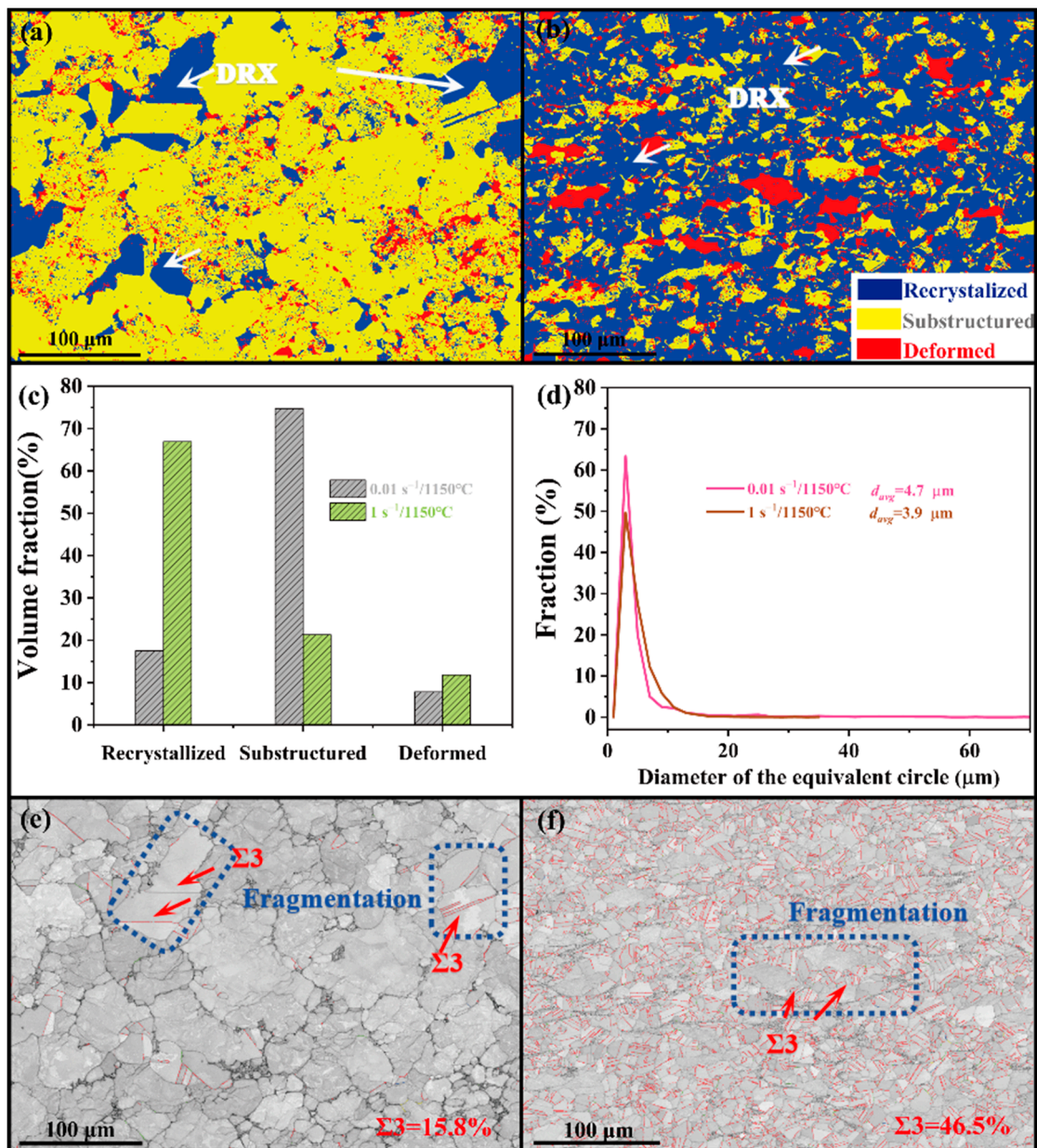


Figure 9. (a) The distribution of recrystallized, substructured, and deformed grains at deformation conditions of $0.01 \text{ s}^{-1}/1150 \text{ }^{\circ}\text{C}$ and (b) $1 \text{ s}^{-1}/1150 \text{ }^{\circ}\text{C}$; (c) Contrast between volume fraction of recrystallized, substructured, and deformed grains at deformation conditions of $0.01 \text{ s}^{-1}/1150 \text{ }^{\circ}\text{C}$ and $1 \text{ s}^{-1}/1150 \text{ }^{\circ}\text{C}$; (d) Average grain diameter at deformation conditions of $0.01 \text{ s}^{-1}/1150 \text{ }^{\circ}\text{C}$ and $1 \text{ s}^{-1}/1150 \text{ }^{\circ}\text{C}$; Band contrast images overlaid with $\Sigma 3$ grain boundaries corresponding to area of (e) Figure 9a and (f) Figure 9b.

The distribution of recrystallized, substructured, and deformed grains at temperatures of $950 \text{ }^{\circ}\text{C}$ and $1050 \text{ }^{\circ}\text{C}$ under a strain rate of 0.1 s^{-1} is illustrated in Figure 8a,b. DRXed grains are predominantly located along the grain boundaries as indicated by white arrows, while fine DRXed grains are observed within the grains as indicated by ovals with white dotted lines. The size of the DRXed grains increases with increasing deformation temperatures. Figure 8c illustrates the comparison of volume fractions for recrystallized, substructured, and deformed grains during hot compression at temperatures of $950 \text{ }^{\circ}\text{C}$ and $1050 \text{ }^{\circ}\text{C}$. It is evident that the proportion of DRXed grains decreases with increasing temperature from 17.41% to 12.73%, while the corresponding volume fraction of substructures decreases from 51.24% to 12.07%. Figure 8d presents the average grain diameter at temperatures of $950 \text{ }^{\circ}\text{C}$

and 1050 °C under a strain rate of 0.1 s⁻¹. The grain diameter increases from 2.9 μm to 3.8 μm as the deformation temperature rises. Figure 8e,f demonstrates the distribution of grain morphology superimposed on Σ3 grain boundaries during deformation at temperatures of 950 °C and 1050 °C with a strain rate of 0.1 s⁻¹. The increase in deformation temperature results in the transformation of previously elongated grains into polygonal shapes, accompanied by a significant enlargement in their dimensions. Moreover, DRXed grains exhibit simultaneous growth patterns with twins evenly distributed along their boundaries. As the temperature rises from 950 °C to 1050 °C, the volume fraction of twin boundaries increases from 14.9% to 20.9%, indicating that more DRXed grains grow and participate in coordinated hot deformation at elevated temperatures. The decrease in the volume fraction of DRX at higher temperatures can be attributed to the suggested increase in the volume fraction of twins resulting from elevated deformation temperatures.

Figure 9a,b illustrates the distribution of recrystallized, substructured, and deformed grains during hot deformation at a temperature of 1150 °C and strain rates of 0.01 s⁻¹ and 1 s⁻¹. Figure 9c presents a comparison of the volume fractions for these three types of grains under the two deformation conditions. The volume fraction of substructured grains reaches a remarkable 74.73% at a strain rate of 0.01 s⁻¹, as depicted in Figure 9a,c. In contrast, the volume fractions for recrystallized and deformed materials are significantly lower, measuring only 17.48% and 7.79%, respectively. The higher volume fraction of the substructure indicates that dislocation motion dominates the deformation at lower strain rates, facilitating enhanced diffusion, and migration of dislocations at elevated temperatures. In contrast, when deformed at a higher strain rate (i.e., 1 s⁻¹), the volume fraction of substructured grains decreases dramatically to only 21.30%, whereas those for a recrystallized and deformed increase to 66.89% and 11.81%, respectively (Figure 9b,c). Additionally, as shown in Figure 9d, the grain size decreases with an increasing strain rate, from 4.7 μm at 0.01 s⁻¹ to 3.9 μm at 1 s⁻¹. Figure 9e,f depicts the distribution of grain morphology overlaid by the Σ3 boundary during hot deformation at a temperature of 1150 °C and strain rates of 0.01 s⁻¹ and 1 s⁻¹, respectively. The impact of an increased strain rate during hot deformation at a temperature of 1150 °C is evident, as it leads to enhanced grain fragmentation and a significant rise in the volume fraction of twins. Specifically, the volume fraction of twins increases from 15.8% at a strain rate of 0.01 s⁻¹ to 46.5% at a strain rate of 1 s⁻¹. The grain refinement can be attributed to the substantial increase in the volume fraction of activated twins participating in the hot deformation process.

3.5. Mechanism of Hot Deformation of the CoCr_{0.4}NiSi_{0.3} Alloy

The XRD pattern of the as-cast CoCr_{0.4}NiSi_{0.3} alloy is depicted in Figure 10a. The XRD patterns of the axial cross-section of the specimens after hot compression under deformation conditions of 0.001 s⁻¹/850 °C, 1 s⁻¹/850 °C, and 1 s⁻¹/1150 °C are presented in Figure 10b. It is evident that the diffraction intensity of the second phase decreases with increasing strain rates and deformation temperatures after hot compression. Moreover, under a hot compression condition of 1 s⁻¹/1150 °C, there is an emergence of additional second phases and an enhancement in the intensity of the HCP structure at 2θ angle of 40.84°. The high-angle annular dark-field scanning transmission electron microscopy (HAADF STEM) images in Figure 11a,b demonstrate the morphological characteristics near grain boundaries under a hot deformation condition of 1 s⁻¹/850 °C. The recrystallized fine grains are primarily distributed along the grain boundaries, with limited occurrence within the grains. The presence of twins and the L₁₂ phase under this deformation condition was confirmed by the analysis of selected area electron diffraction (SAED), as depicted in Figure 11c. The energy dispersive spectrum (EDS), shown in Figure 11e–h, corresponds to the dark field image region displayed in Figure 11d, where B represents the intragranular DRXed grain. The EDS analysis revealed that the average chemical composition of the DRXed grains, denoted as 1, 2, and 3, was determined to be 18.30 Co–1.92 Cr–53.49 Ni–26.27 Si (at.%). The SAED analysis was conducted on region A of the matrix depicted in Figure 11b, as illustrated in Figure 11i. The crystallographic plane indicated by the red

circle has been confirmed to be in the $L1_2$ phase, and the fast Fourier transformed (FFT) image of the $L1_2$ phase is presented in Figure 11j.

The deformation condition leads to the precipitation of the granular $L1_2$ phase with an approximate diameter range of 10–20 nm within the matrix. Furthermore, it can be inferred that under a deformation condition of $1\text{ s}^{-1}/850\text{ }^\circ\text{C}$, recrystallized grains exhibit the HCP phase internally as well as at the interfaces between grains. Additionally, the hot deformation is also mediated by twins.

Figure 12a depicts the morphology of primary and secondary twins in the deformed grains of the FCC matrix under a processing condition of $0.001\text{ s}^{-1}/850\text{ }^\circ\text{C}$, while Figure 12b presents a high-resolution image of region B indicated in Figure 12a. SAED images reveal the presence of double twins and the $L1_2$ phase in Figure 12b. The initiation of double twins is strongly correlated with the oscillation curve depicted in Figure 2a. The materials with high Q exhibit relatively slower kinetics of DRX [47]. The role of twins in the nucleation and growth of DRX has been widely acknowledged [43]. Furthermore, materials with low SFE are prone to initiating DDRX [42], thereby suggesting that double twins facilitate deformation. In Figure 12c, an abundance of dislocations and twins surrounding the recrystallized grains can be observed. The entangled dislocations obstruct the grain and promote twin formation upon reaching the required critical stress, initiating multiple slip systems that facilitate hot deformation. In Figure 12d, the morphology of a regular arrangement of lamellar structures was observed in the recrystallized grains of the HCP phase under a deformation condition of $1\text{ s}^{-1}/850\text{ }^\circ\text{C}$. In Figure 12e,f, the recrystallized grains of the HCP phase exhibited a presence of lamellar superlattice structure under a deformation condition of $0.001\text{ s}^{-1}/850\text{ }^\circ\text{C}$. The EDS analysis was conducted at a deformation condition of $0.001\text{ s}^{-1}/850\text{ }^\circ\text{C}$, revealing the chemical composition of the DRXed HCP phase was 17.78 Co–2.03 Cr–54.10 Ni–26.09 Si (at.%), indicating an abundance in Ni and Si. The SAED analysis indicated the existence of a well-defined long-period stacking order (LPSO) structure. The obtained LPSO phase originates from DRX induced by hot deformation, wherein the solubility of Si and Ni decreases with increasing temperature, resulting in their rearrangement into an ordered structure within a localized region during the process of DRXed grain formation. The phase type of LPSO in this MEA during deformation requires further validation through more comprehensive and systematic research. In addition to being located within the DRXed HCP grains, Figure 13a illustrates the presence of lamellar LPSO structure in localized regions of the FCC matrix under deformation conditions of $0.001\text{ s}^{-1}/850\text{ }^\circ\text{C}$. In Figure 13b, a detailed view of region E from Figure 13a is presented, while Figure 13c displays the corresponding electron diffraction pattern. Additionally, Figure 13d illustrates the electron diffraction pattern specifically obtained from region E shown in Figure 13b, and the inverse fast Fourier transform (IFFT) diagram of the crystallographic plane circled in green in Figure 13d is illustrated in Figure 13e. The spacing of the crystallographic plane marked in green of the LPSO structure was measured to be 2.97 Å. Figure 13b,e indicates the existence of a stacking fault (SF) transition region at the edge of LPSO. The images in Figure 13f,i were acquired from the “good region” and “transition region” of the LPSO structure, respectively. The corresponding fast Fourier transform (FFT) is depicted in Figure 13g,j, while the inverse fast Fourier transform (IFFT) of the corresponding crystallographic plane is illustrated in Figure 13h,k. In Figure 13g, weak-intensity diffraction spots indicate the presence of the $L1_2$ phase. Figure 13i,k presents images of LPSO and its transition structure confirmed as SFs in region E. The transition of LPSO in this MEA is inferred to occur through the rearrangement of SFs within the FCC matrix during hot deformation, which can be attributed to its low SFE. This transition is induced by hot compression and results in a transformation to the HCP phase before further transitioning into the LPSO structure with solute redistribution. Apart from work hardening as a strengthening factor, twin initiation combined with second-phase particles such as LPSO and $L1_2$ contributes to maintaining high flow stress under these deformation conditions.

Figure 14a depicts the morphology of twins in recrystallized grains at $1 \text{ s}^{-1}/1150 \text{ }^\circ\text{C}$, while Figure 14b demonstrates the presence of dislocations and serrated grain boundaries within the recrystallized grain, indicating the experience of elevated local flow stress. The EDS analysis was conducted at a deformation condition of $1 \text{ s}^{-1}/1150 \text{ }^\circ\text{C}$, revealing the chemical composition of the DRXed phase was 20.14 Co–2.51 Cr–54.08 Ni–23.28 Si (at.%). The volume fractions of recrystallized and substructured grains in Figure 9c are confirmed as 66.89% and 21.30%, respectively, while the volume fraction of $\Sigma 3$ grain boundary in Figure 9f is determined to be 46.5%. Elevated strain rates and deformation temperatures result in elevated volume fractions of DRX and dislocations. As the DRXed grains continue to grow, they actively contribute to deformation by generating dislocations and promoting deformation twinning. The diffraction pattern observed in Figure 14d corresponds to region A as depicted in Figure 14c, demonstrating the presence of twins. Similarly, the diffraction pattern shown in Figure 14e corresponds to region B in Figure 14c. In addition to the FCC matrix, it can be inferred from Figure 14e that the $L1_2$ phase is coherent with the matrix. Moreover, a high-resolution image of region A from Figure 14c is presented in Figure 14f, while an enlarged high-resolution image of region C is displayed in Figure 14g. Finally, the FFT analysis of the region depicted in Figure 14g is illustrated in Figure 14h. Based on Figure 14d,f–h, it can be concluded that apart from twins, SFs, and LPSO structures that are coherent within the FCC matrix, there exist coherent superlattice structures within region A. These superlattice structures form at a temperature resistance level of $1 \text{ s}^{-1}/1150 \text{ }^\circ\text{C}$. The thickness of the LPSO lamellae decreases with increasing temperature, ranging from 16 nm at $850 \text{ }^\circ\text{C}$ (Figure 13a) to 4–8 nm at $1150 \text{ }^\circ\text{C}$ (Figure 14g). The occurrence and transformation of the LPSO phase indicate its metastable nature, which is influenced by both temperature and stress and is accompanied by twinning and SFs.

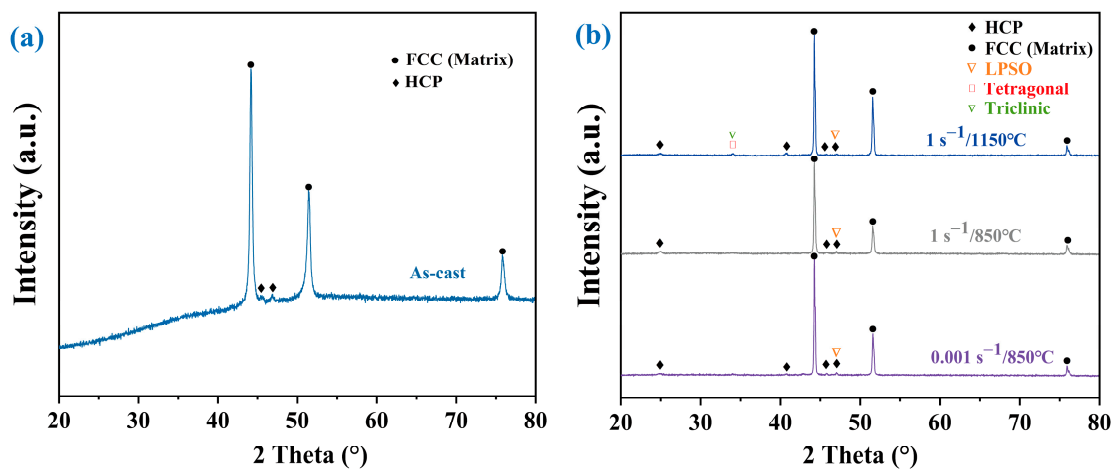


Figure 10. (a) XRD pattern of the as-cast $\text{CoCr}_{0.4}\text{NiSi}_{0.3}$ alloy; (b) XRD patterns of the $\text{CoCr}_{0.4}\text{NiSi}_{0.3}$ alloy hot compressed at $0.001 \text{ s}^{-1}/850 \text{ }^\circ\text{C}$, $1 \text{ s}^{-1}/850 \text{ }^\circ\text{C}$, and $1 \text{ s}^{-1}/1150 \text{ }^\circ\text{C}$.

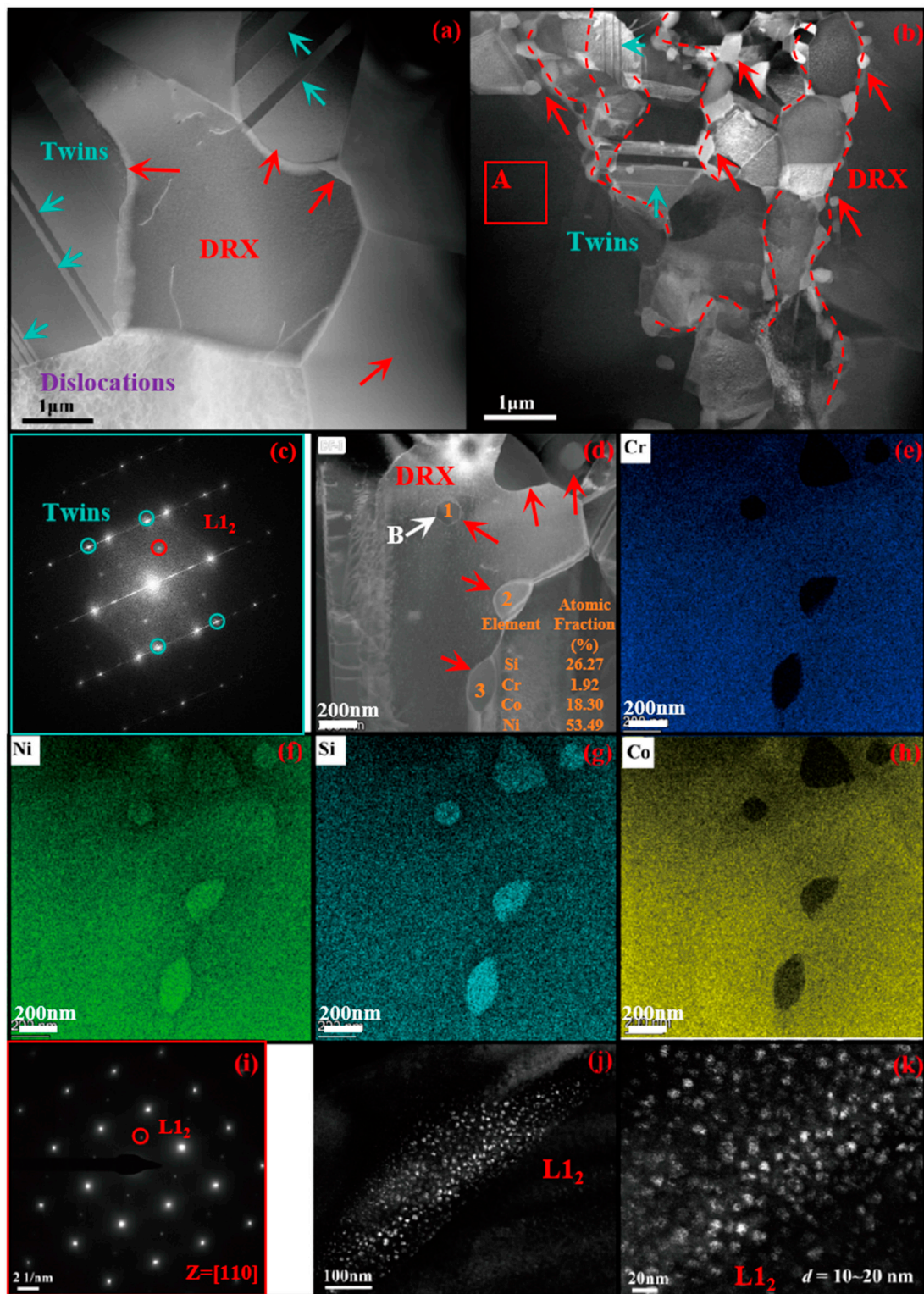


Figure 11. (a) The HAADF STEM images reveal the morphology of grain boundaries with twins under a deformation condition of $1 \text{ s}^{-1}/850 \text{ }^\circ\text{C}$; (b,d) The HAADF STEM images reveal the morphology of grain boundaries under a deformation condition of $1 \text{ s}^{-1}/850 \text{ }^\circ\text{C}$; (c) The SAED of Figure 11a; (d) The intragranular DRXed grain B and the atomic fraction of DRXed grains under a deformation condition of $1 \text{ s}^{-1}/850 \text{ }^\circ\text{C}$; (e–h) EDS of the region corresponding to Figure 11d; (i) The SAED of region A in Figure 11b; (j) The FFT of $L1_2$ in Figure 11i; (k) The enlarged image of $L1_2$ in Figure 11j.

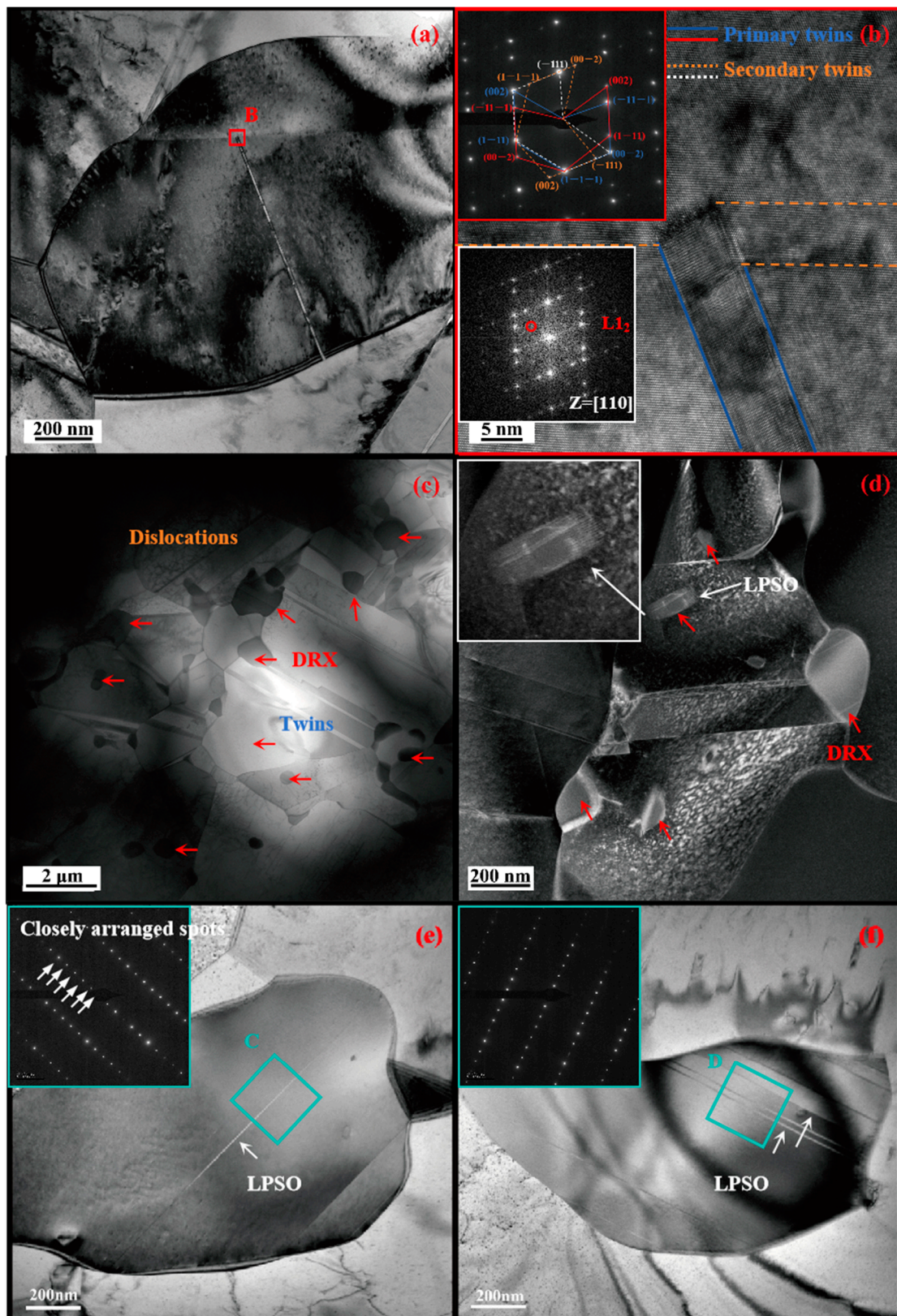


Figure 12. (a) Dark field images of double twins morphology under hot deformation condition of $0.001 \text{ s}^{-1}/850 \text{ }^\circ\text{C}$; (b) High-resolution image of region B in Figure 12a; The microstructural morphologies near grain boundaries at (c) $0.001 \text{ s}^{-1}/850 \text{ }^\circ\text{C}$, and (d) $1 \text{ s}^{-1}/850 \text{ }^\circ\text{C}$; (e,f) The microstructural morphologies of DRX at $0.001 \text{ s}^{-1}/850 \text{ }^\circ\text{C}$ exhibit the LPSO structure.

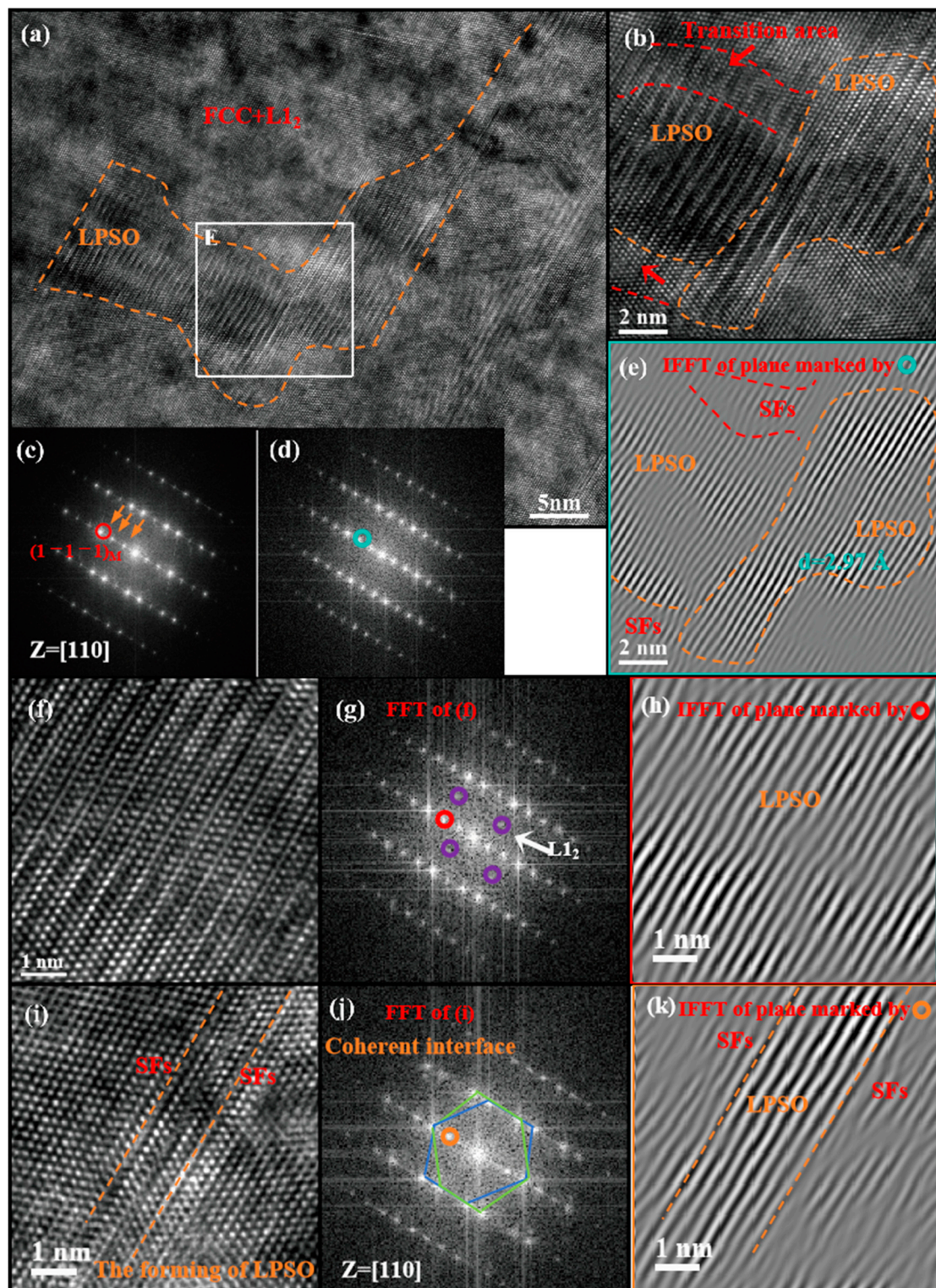


Figure 13. (a) The high-resolution image of LPSO structure under deformation condition of $0.001 \text{ s}^{-1}/850 \text{ }^{\circ}\text{C}$; (b) The enlarged region E of Figure 13a; (c) The FFT of Figure 13a; (d) The FFT of Figure 13b; (e) The IFFT of crystallographic plane circled in green in Figure 13d; (f) The “good region” of LPSO structure from Figure 13b; (g) The FFT of Figure 13f demonstrates the presence of the $L1_2$ phase; (h) The IFFT of crystallographic plane circled in red in Figure 13g; (i) The “transition region” of the LPSO structure from Figure 13b; (j) The FFT of Figure 13i demonstrates the coherent relationship between the matrix, twins, and LPSO phase; (k) The IFFT of crystallographic plane circled in yellow in Figure 13j.

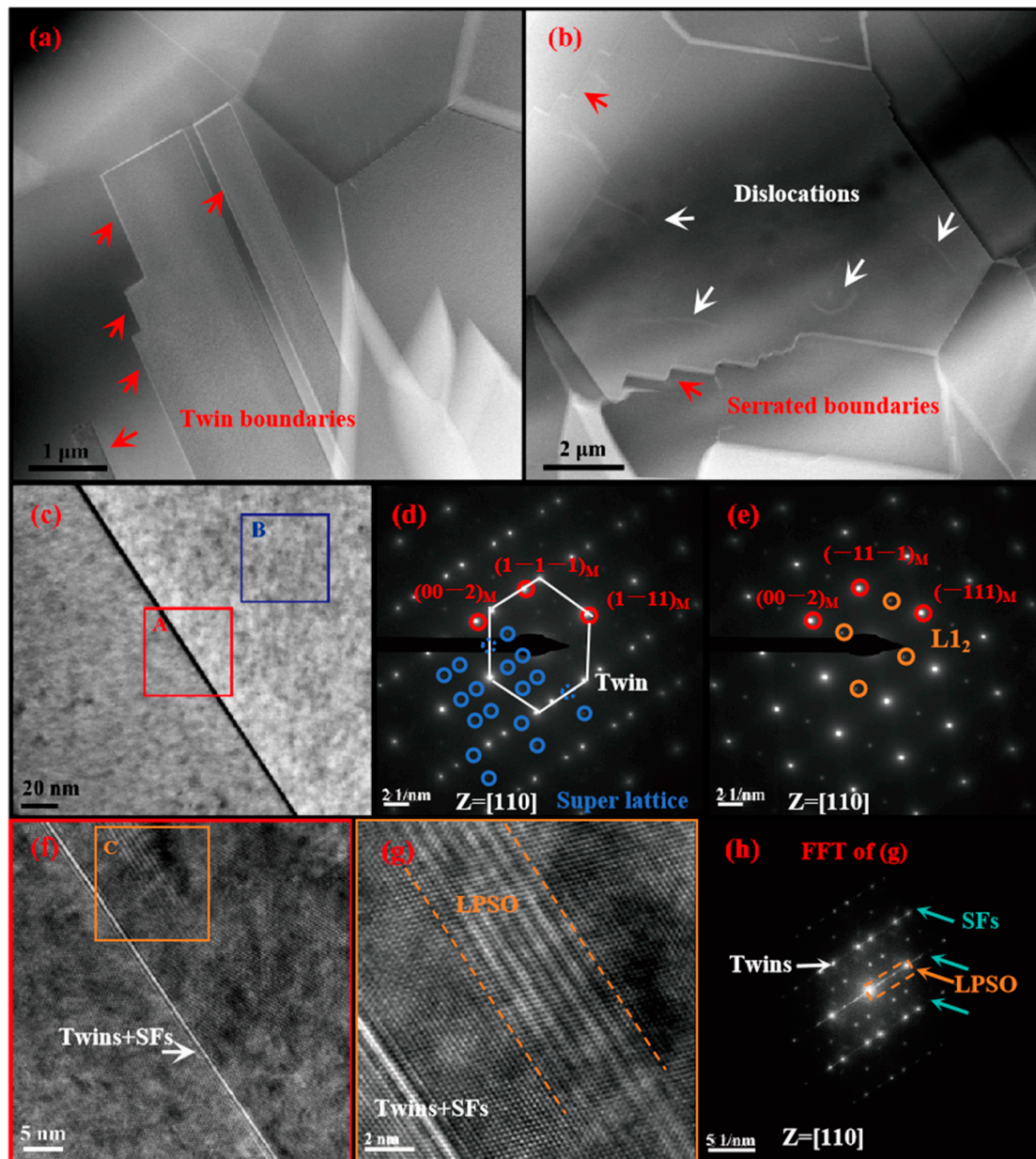


Figure 14. (a) Twin boundaries in DRXed grains; (b) Serrated boundaries in DRXed grains; (c) Morphologies under a hot deformation condition of $1 \text{ s}^{-1}/1150 \text{ }^{\circ}\text{C}$; (d) SAED of region A in Figure 14c; (e) SAED of region B in Figure 14c; (f) The high-resolution image of region A in Figure 14c; (g) Enlarged area of region C in Figure 14f; (h) The FFT of Figure 14g.

Based on the structural characterization under various deformation conditions, the formation and growth of DRX in this MEA can be attributed to the interaction between dislocations, twins, and second phases such as the L_{12} phase, and LPSO phase, which significantly influence the flow stress and grain size during hot deformation. Dislocation slip is significantly impeded by grain boundaries during hot compression, leading to dislocation entrapment at interfaces. Therefore, DRXed grains preferentially nucleate at grain boundaries. However, as the strain rate decreases and deformation temperature increases, the nucleation sites facilitated by grain boundaries become inadequate. Therefore, DRXed grains initiate growth at the interface of the LPSO phase as depicted in Figure 12c. At high strain rates, the recrystallization process leads to the formation of the LPSO phase in the DRXed grains. Figure 12d illustrates the observation of HCP-DRX within the lamellar LPSO phase. Moreover, under a strain rate of 0.001 s^{-1} , the SFs in the FCC matrix transform to the

HCP phase during deformation and subsequently form LPSO, as depicted in Figure 13i–k. Following the law of FCC–HCP phase transition of this MEA [55], the generated LPSO phase can follow either process due to low SFE: FCC→SFs→HCP→LPSO produced by SFs, or FCC→Twins→HCP→LPSO produced by twinning. The recrystallization process at high strain rates results in the formation of the lamellar LPSO phase within the DRXed grains as shown in Figure 12d. Additionally, under a strain rate of 0.001 s^{-1} , deformation causes the transformation of SFs in the FCC matrix into the HCP phase, subsequently leading to LPSO formation, as depicted in Figure 13i–k. Following the FCC–HCP phase transition law in this MEA [55], the generated LPSO phase can nucleate through either process due to low SFE [56] of this CoCrNi-based MEA followed the process of FCC→SFs→HCP→LPSO produced by SFs or FCC→Twins→HCP→LPSO produced by twinning. The LPSO phase, being a hard precipitated phase, exhibits a dispersion-strengthening effect during deformation. It effectively hinders dislocation slip and acts as nucleation sites for recrystallized grains, as depicted in Figure 14b. The zigzag interface facilitates the process of recrystallization and further accommodates dislocations to alleviate local stress during continuous deformation, thereby reducing the extent of DRX. The interactions between dislocations and deformation twins, second phases coherent with the FCC matrix such as $L1_2$, LPSO, and superlattice structures formed through phase transition contribute to the delayed occurrence of instability that is confined to localized regions.

4. Conclusions

This study investigated the hot deformation behavior and microstructural evolution of $\text{CoCr}_{0.4}\text{NiSi}_{0.3}$ MEA within a temperature range of $850\text{--}1150\text{ }^\circ\text{C}$ and strain rates ranging from $0.001\text{--}1\text{ s}^{-1}$. This study elucidates the underlying mechanisms governing DRX and strengthening of the MEA, thereby reaching the following conclusions:

- (1) The peak stress increases with the rise in strain rate and decreases with elevated deformation temperature under hot deformation conditions of $0.001\text{--}1\text{ s}^{-1}/850\text{--}1150\text{ }^\circ\text{C}$. The high-temperature activation energy (Q) of the MEA is determined to be 423.6602 kJ/mol . The constitutive equation of this MEA for hot deformation, based on the Arrhenius-type hyperbolic sine formula, can be expressed as follows:

$$\dot{\epsilon} = 2.0052 \times 10^{15} [\sinh(0.0059\sigma)]^{3.8376} \exp\left(-\frac{423660.2}{RT}\right)$$

- (2) The numerical value of η increases with increasing of the true strain. The region of instability is observed exclusively when the true strain surpasses 0.4 in this investigation. At true strains ranging from 0.4 to 0.7, the instability regions are observed at temperatures ranging from $850\text{--}890\text{ }^\circ\text{C}$, accompanied by corresponding strain rates of $0.1\text{--}0.7\text{ s}^{-1}$. The suitable range of parameters for hot-working decreases as the true strain increases. The regions of instability observed on the hot processing map are in accordance with the experimental findings.
- (3) The volume fraction of DRX decreases with increasing strain rate, while the average grain size decreases. The volume fraction of DRX diminishes with rising temperature, leading in increased grain size. Twins mediate deformation during hot processing, resulting in grain refinement and enhanced flow stress. In the temperature range of $850\text{--}1050\text{ }^\circ\text{C}$, an inverse correlation is observed between the volume fraction of twins and DRX due to enhanced hot deformation and the initiation of a multi-slip system for flow stress mitigation. The growth of deformation twins during recrystallization at $1150\text{ }^\circ\text{C}$ is in accordance with the trend of volume fraction of twins and recrystallization, indicating an enhanced volume of DRXed grains that undergo coordinated hot deformation at elevated temperatures.
- (4) The TEM characterization elucidated the DRX mechanism in this MEA. The presence of the LPSO phase was observed in both the FCC matrix and HCP recrystallized grains under various deformation conditions, with similar chemical compositions enriched in nickel and silicon atoms. Specifically, the LPSO phase forms from the

matrix at a low strain rate, while it emerges during recrystallization at a high strain rate. The phase type of LPSO in this MEA during deformation necessitates further validation through more comprehensive and systematic research.

- (5) The increased flow stress of the as-cast MEA can be primarily attributed to interactions between dislocations and twins, as well as second phases such as $L1_2$, LPSO, and superlattice structures formed by phase transitions that are coherent with the matrix during hot compression. These factors elucidate the occurrence of instability at a later stage within a narrow range. The second phase acts as a nucleation site for recrystallization and contributes to dispersion-strengthening. Furthermore, their interaction with dislocations influences flow stress and the process of recrystallization during hot deformation.

Author Contributions: Conceptualization, L.Z. and W.Z.; methodology, L.Z.; software, L.Z.; validation, L.Z., L.C., F.L. and H.Z. (Hui Zhao); formal analysis, L.Z.; investigation, G.Z. and H.Z. (Haoyu Zhang); resources, L.Z.; data curation, L.Z., G.Z. and N.G.; writing—original draft preparation, L.Z. and F.L.; writing—review and editing, L.Z.; visualization, L.Z.; supervision, H.Z. (Hui Zhao), W.Z., F.L. and L.C.; project administration, H.Z. (Hui Zhao) and L.Z.; funding acquisition, L.Z. All authors have read and agreed to the published version of the manuscript.

Funding: The authors would like to gratefully acknowledge the support received from the Basic Scientific Research Projects for colleges and universities (General Programs), funded by the Education Department of Liaoning Province of China (No. LJKMZ20220592).

Informed Consent Statement: Not applicable.

Data Availability Statement: The data presented in this study are available on request from the corresponding author. The data are not publicly available due to privacy.

Conflicts of Interest: The authors declare no conflict of interest.

References

1. Yeh, J.W.; Chen, S.K.; Lin, S.J.; Gan, J.Y.; Chin, T.S.; Shun, T.T.; Tsau, C.-H.; Chang, S.-Y. Nanostructured High-entropy alloys with multiple principal elements: Novel Alloy Design Concepts and Outcomes. *Adv. Eng. Mater.* **2004**, *6*, 299–303. [\[CrossRef\]](#)
2. Cantor, B.; Chang, I.T.H.; Knight, P.; Vincent, A.J.B. Microstructural development in equiatomic multicomponent alloys. *Mater. Sci. Eng. A* **2004**, *375–377*, 213–218. [\[CrossRef\]](#)
3. Dong, Y.; Zhou, K.; Lu, Y.; Gao, X.; Wang, T.; Li, T. Effect of vanadium addition on the microstructure and properties of AlCoCrFeNi high entropy alloy. *Mater. Des.* **2014**, *57*, 67–72. [\[CrossRef\]](#)
4. Chen, J.; Niu, P.; Liu, Y.; Lu, Y.; Wang, X.; Peng, Y.; Liu, J. Effect of zr content on microstructure and mechanical properties of AlCoCrFeNi High Entropy Alloy. *Mater. Des.* **2016**, *94*, 39–44. [\[CrossRef\]](#)
5. Han, Z.D.; Chen, N.; Zhao, S.F.; Fan, L.W.; Yang, G.N.; Shao, Y.; Yao, K.F. Effect of Ti additions on mechanical properties of NbMoTaW and VNbMoTaW refractory high entropy alloys. *Intermetallics* **2017**, *84*, 153–157. [\[CrossRef\]](#)
6. Fan, Q.C.; Li, B.S.; Zhang, Y. Influence of Al and Cu elements on the microstructure and properties of (FeCrNiCo)AlxCu_y high-entropy alloys. *J. Alloys Compd.* **2014**, *614*, 203–210. [\[CrossRef\]](#)
7. Juan, C.-C.; Tseng, K.-K.; Hsu, W.-L.; Tsai, M.-H.; Tsai, C.-W.; Lin, C.-M.; Chen, S.-K.; Lin, S.-J.; Yeh, J.-W. Solution strengthening of ductile refractory HfMoxNbTaTiZr high-entropy alloys. *Mater. Lett.* **2016**, *175*, 284–287. [\[CrossRef\]](#)
8. Xie, Y.; Cheng, H.; Tang, Q.; Chen, W.; Chen, W.; Dai, P. Effects of N addition on microstructure and mechanical properties of CoCrFeNiMn high entropy alloy produced by mechanical alloying and Vacuum Hot Pressing Sintering. *Intermetallics* **2018**, *93*, 228–234. [\[CrossRef\]](#)
9. Wang, Z.; Baker, I.; Cai, Z.; Chen, S.; Poplawsky, J.D.; Guo, W. The effect of interstitial carbon on the mechanical properties and dislocation substructure evolution in Fe_{40.4}Ni_{11.3}Mn_{34.8}Al_{7.5}Cr₆ high entropy alloys. *Acta Mater.* **2016**, *120*, 228–239. [\[CrossRef\]](#)
10. Qiao, L.; Zhu, J. Constitutive modeling of hot deformation behavior of AlCrFeNi multi-component alloy. *Vacuum* **2022**, *201*, 111059. [\[CrossRef\]](#)
11. Yao, H.W.; Qiao, J.W.; Gao, M.C.; Hawk, J.A.; Ma, S.G.; Zhou, H.F.; Zhang, Y. NbTaV-(Ti,W) refractory high-entropy alloys: Experiments and modeling. *Mater. Sci. Eng. A* **2016**, *674*, 203–211. [\[CrossRef\]](#)
12. Jang, M.J.; Ahn, D.-H.; Moon, J.; Bae, J.W.; Yim, D.; Yeh, J.-W.; Estrin, Y.; Kim, H.S. Constitutive modeling of deformation behavior of high-entropy alloys with face-centered cubic crystal structure. *Mater. Res. Lett.* **2017**, *5*, 350–356. [\[CrossRef\]](#)
13. Castin, N.; Malerba, L.; Bonny, G.; Pascuet, M.I.; Hou, M. Modelling radiation-induced phase changes in binary FeCu and ternary FeCuNi alloys using an artificial intelligence-based atomistic kinetic Monte Carlo approach. *Nucl. Instrum. Methods Phys. Res. Sect. B* **2009**, *267*, 3002–3008. [\[CrossRef\]](#)

14. Gao, M.C.; Gao, P.; Hawk, J.A.; Ouyang, L.; Alman, D.E.; Widom, M. Computational modeling of high-entropy alloys: Structures, thermodynamics and Elasticity. *J. Mater. Res.* **2017**, *32*, 3627–3641. [[CrossRef](#)]
15. Jin, X.; Liang, Y.; Bi, J.; Li, B. Enhanced strength and ductility of Al_{0.9}CoCrNi_{2.1} eutectic high entropy alloy by thermomechanical processing. *Materialia* **2020**, *10*, 100639. [[CrossRef](#)]
16. Stepanov, N.D.; Shaysultanov, D.G.; Chernichenko, R.S.; Yurchenko, N.Y.; Zhrebtsov, S.V.; Tikhonovsky, M.A.; Salishchev, G.A. Effect of thermomechanical processing on microstructure and mechanical properties of the carbon-containing CoCrFeNiMn high entropy alloy. *J. Alloys Compd.* **2017**, *693*, 394–405. [[CrossRef](#)]
17. Cheng, H.; Wang, H.Y.; Xie, Y.C.; Tang, Q.H.; Dai, P.Q. Controllable fabrication of a carbide-containing FeCoCrNiMn high-entropy alloy: Microstructure and mechanical properties. *Mater. Sci. Technol.* **2017**, *33*, 2032–2039. [[CrossRef](#)]
18. Gao, N.; Lu, D.H.; Zhao, Y.Y.; Liu, X.W.; Liu, G.H.; Wu, Y.; Liu, G.; Fan, Z.T.; Lu, Z.P.; George, E.P. Strengthening of a CrMnFeCoNi high-entropy alloy by carbide precipitation. *J. Alloys Compd.* **2019**, *792*, 1028–1035. [[CrossRef](#)]
19. Sun, S.J.; Tian, Y.Z.; Lin, H.R.; Dong, X.G.; Wang, Y.H.; Zhang, Z.J.; Zhang, Z.F. Enhanced strength and ductility of bulk CoCrFeMnNi high entropy alloy having fully recrystallized ultrafine-grained structure. *Mater. Des.* **2017**, *133*, 122–127. [[CrossRef](#)]
20. Dan Sathiaraj, G.; Skrotzki, W.; Pukenas, A.; Schaarschuch, R.; Jose Immanuel, R.; Panigrahi, S.K.; Arout Chelvane, J.; Satheesh Kumar, S.S. Effect of annealing on the microstructure and texture of cold rolled CrCoNi medium-entropy alloy. *Intermetallics* **2018**, *101*, 87–98. [[CrossRef](#)]
21. Gludovatz, B.; Hohenwarter, A.; Thurston, K.V.; Bei, H.; Wu, Z.; George, E.P.; Ritchie, R.O. Exceptional damage-tolerance of a medium-entropy alloy CrCoNi at cryogenic temperatures. *Nat. Commun.* **2016**, *7*, 10602. [[CrossRef](#)] [[PubMed](#)]
22. Qiu, S.; Zheng, G.P.; Jiao, Z.B. Alloying effects on phase stability, mechanical properties, and deformation behavior of CoCrNi-based medium-entropy alloys at low temperatures. *Intermetallics* **2022**, *140*, 107399. [[CrossRef](#)]
23. Ding, Q.; Fu, X.; Chen, D.; Bei, H.; Gludovatz, B.; Li, J.; Zhang, Z.; George, E.P.; Yu, Q.; Zhu, T.; et al. Real-time nanoscale observation of deformation mechanisms in CrCoNi-based medium- to high-entropy alloys at cryogenic temperatures. *Mater. Today* **2019**, *25*, 21–27. [[CrossRef](#)]
24. Shi, C.X.; Du, X.H.; Zhang, J.Y.; Duan, G.S.; Yang, M.C.; Zu, R.F.; Li, W.P.; Chou, T.H.; Wu, B.L.; Sun, J.; et al. Superb strength-ductility synergy in a medium-entropy CoCrNi alloy via reinforced trip effect. *J. Mater. Res. Technol.* **2022**, *20*, 104–113. [[CrossRef](#)]
25. Chang, H.; Zhang, T.W.; Ma, S.G.; Zhao, D.; Xiong, R.L.; Wang, T.; Li, Q.; Wang, Z.H. Novel Si-added CrCoNi medium entropy alloys achieving the breakthrough of strength-ductility trade-off. *Mater. Des.* **2021**, *197*, 109202. [[CrossRef](#)]
26. Dharmendra, C.; Rao, K.P.; Zhao, F.; Prasad, Y.V.R.K.; Hort, N.; Kainer, K.U. Effect of silicon content on hot working, processing maps, and microstructural evolution of cast TX32–0.4Al Magnesium alloy. *Mater. Sci. Eng. A* **2014**, *606*, 11–23. [[CrossRef](#)]
27. An, N.; Sun, Y.; Wu, Y.; Tian, J.; Li, Z.; Li, Q.; Chen, J.; Hui, X. High temperature strengthening via nanoscale precipitation in Wrought CoCrNi-based medium-entropy alloys. *Mater. Sci. Eng. A* **2020**, *798*, 140213. [[CrossRef](#)]
28. Yang, R.; Yang, L.; Wang, T.; Wang, Q. Enhanced strength and crack resistance in CoCrNi-based medium entropy alloy with nano-precipitates, 9R structures and nanotwins produced by hot isostatic pressing. *Intermetallics* **2023**, *159*, 107929. [[CrossRef](#)]
29. Yi, H.; Wei, D.; Wang, Y.; Wang, L.; Fang, M.; Yang, K.; Kato, H. Hot deformation and dynamic recrystallization behavior of CoCrNi and (CoCrNi)₉₄Ti₃Al₃ medium entropy alloys. *Metals* **2020**, *10*, 1341. [[CrossRef](#)]
30. Wang, H.; Hu, Z.; Cao, J.; Zhang, S.; Cheng, T.; Wang, Q. Hot deformation and workability of a CrCoNi medium entropy alloy. *Met. Mater. Int.* **2021**, *28*, 514–522. [[CrossRef](#)]
31. Ebrahimian, M.; Rizi, M.S.; Hong, S.I.; Kim, J.H. Effects of molybdenum on hot deformation behavior and microstructural evolution of Fe₄₀Mn₄₀Co₁₀Cr₁₀0.5 high entropy alloys. *Sci. Technol. Adv. Mater.* **2023**, *24*, 2186119. [[CrossRef](#)] [[PubMed](#)]
32. Sauza, D.J.; Dunand, D.C.; Noebe, R.D.; Seidman, D.N. γ' -(L₁₂) precipitate evolution during isothermal aging of a CoAlWNi Superalloy. *Acta Mater.* **2019**, *164*, 654–662. [[CrossRef](#)]
33. Goodfellow, A.J.; Galindo-Nava, E.I.; Christofidou, K.A.; Jones, N.G.; Boyer, C.D.; Martin, T.L.; Bagot, P.A.J.; Hardy, M.C.; Stone, H.J. The effect of phase chemistry on the extent of strengthening mechanisms in model Ni-Cr-Al-Ti-Mo based superalloys. *Acta Mater.* **2018**, *153*, 290–302. [[CrossRef](#)]
34. Chen, D.; He, F.; Han, B.; Wu, Q.; Tong, Y.; Zhao, Y.; Wang, Z.; Wang, J.; Kai, J. Synergistic effect of Ti and Al on L₁₂-phase design in CoCrFeNi-based high entropy alloys. *Intermetallics* **2019**, *110*, 106476. [[CrossRef](#)]
35. Sato, H.; Toth, R.S.; Honjo, G. Long period stacking order in close packed structures of Metals. *J. Phys. Chem. Solids* **1967**, *28*, 137–160. [[CrossRef](#)]
36. Hu, J.; Zhang, X.; Tang, C.; Deng, Y.; Liu, Z.; Yang, L. Microstructures and mechanical properties of the Mg–8Gd–4Y–Nd–Zn–3Si (wt%) alloy. *Mater. Sci. Eng. A* **2013**, *571*, 19–24. [[CrossRef](#)]
37. Zhao, D.; Chen, X.; Ye, J.; Chen, T.; Dai, Y.; Liu, C.; Luo, Z.; Gao, S.; Zhang, J.; Yao, J.; et al. Simultaneously improving elastic modulus and damping capacity of extruded MG-gd-y-zn-mn alloy via alloying with si. *J. Alloys Compd.* **2019**, *810*, 151857. [[CrossRef](#)]
38. Li, J.; Wang, F.; Zeng, J.; Zhao, C.; Jin, L.; Dong, J. Effect of the interspacing of intragranular lamellar LPSO phase on dynamic recrystallization behaviors of Mg-Gd-Y-Zn-Zr alloys. *Mater. Charact.* **2022**, *193*, 112326. [[CrossRef](#)]
39. Wang, Z.; Jiang, C.; Fang, Q.; Liu, F.; Liu, B.; Fan, T.; Ma, L.; Tang, P. First-principles exploration of the stabilization mechanism of long-period stacking ordered structures in high performance Al Alloys. *Prog. Nat. Sci. Mater. Int.* **2020**, *30*, 424–431. [[CrossRef](#)]

40. Zheng, G.; Tang, B.; Zhao, S.; Xie, Y.; Wang, W.Y.; Li, J.; Zhu, L. Novel deformation mechanism of nanolamellar microstructure and its effect on mechanical properties of TiAl Intermetallics. *Mater. Sci. Eng. A* **2023**, *879*, 145138. [[CrossRef](#)]
41. Song, Y.; Li, Y.; Zhao, G.; Liu, H.; Li, H.; Li, J.; Liu, E. Electron backscatter diffraction investigation of heat deformation behavior of 2205 duplex stainless steel. *Steel Res. Int.* **2021**, *92*, 2000587. [[CrossRef](#)]
42. Emdadi, A.; Stryzhyboroda, O.; Hecht, U.; Bambach, M. Complex dynamic restoration processes leading to a high degree of deformability in a dual-phase Al_{0.5}CoCrFeNi high entropy alloy. *J. Alloys Compd.* **2022**, *918*, 165583. [[CrossRef](#)]
43. Ponge, D.; Gottstein, G. Necklace formation during dynamic recrystallization: Mechanisms and impact on flow behavior. *Acta Mater.* **1998**, *46*, 69–80. [[CrossRef](#)]
44. Imran, S.M.; Li, C.; Lang, L.; Guo, Y.; Mirza, H.A.; Haq, F.; Alexandrova, S.; Jiang, J.; Han, H. An investigation into arrhenius type constitutive models to predict complex hot deformation behavior of TC4 alloy having bimodal microstructure. *Mater. Today Commun.* **2022**, *31*, 103622. [[CrossRef](#)]
45. Sellars, C.M.; McTegart, W.J. On the mechanism of hot deformation. *Acta Metall.* **1966**, *14*, 1136–1138. [[CrossRef](#)]
46. Wang, Y.-T.; Li, J.-B.; Xin, Y.-C.; Chen, X.-H.; Rashad, M.; Liu, B.; Liu, Y. Hot deformation behavior and hardness of a CoCrFeMnNi high-entropy alloy with high content of carbon. *Acta Metall. Sin. (Engl. Lett.)* **2019**, *32*, 932–943. [[CrossRef](#)]
47. Annasamy, M.; Haghdadi, N.; Taylor, A.; Hodgson, P.; Fabijanic, D. Dynamic recrystallization behaviour of Al_xCoCrFeNi high entropy alloys during high-temperature plane strain compression. *Mater. Sci. Eng. A* **2019**, *745*, 90–106. [[CrossRef](#)]
48. Chen, X.; Liao, Q.; Niu, Y.; Jia, W.; Le, Q.; Cheng, C.; Yu, F.; Cui, J. A constitutive relation of az80 magnesium alloy during hot deformation based on Arrhenius and Johnson–Cook Model. *J. Mater. Res. Technol.* **2019**, *8*, 1859–1869. [[CrossRef](#)]
49. Zener, C.; Hollomon, J. Effect of strain rate upon plastic flow of steel. *J. Appl. Phys.* **1944**, *15*, 22–32. [[CrossRef](#)]
50. Raj, R. Development of a processing map for use in warm-forming and hot-forming processes. *Metall. Mater. Trans. A* **1981**, *12*, 1089–1097. [[CrossRef](#)]
51. Prasad, Y.V.; Gegel, H.L.; Doraivelu, S.M.; Malas, J.C.; Morgan, J.T.; Lark, K.A.; Barker, D.R. Modeling of dynamic material behavior in hot deformation: Forging of Ti-6242. *Metall. Mater. Trans. A* **1984**, *15*, 1883–1892. [[CrossRef](#)]
52. Srinivasa, N.; Prasad, Y.V.R.K. Hot working characteristics of nimonic 75, 80A and 90 superalloys: A comparison using processing maps. *J. Mater. Process. Technol.* **1995**, *51*, 171–192. [[CrossRef](#)]
53. Prasad, Y.V.R.K. Recent advances in the science of mechanical processing. *Indian J. Technol.* **1990**, *28*, 435–451.
54. Prasad, Y.V.R.K.; Seshacharyulu, T. Processing maps for hot working of titanium alloys. *Mater. Sci. Eng. A* **1998**, *243*, 82–88. [[CrossRef](#)]
55. Zhang, L.; Zhang, W.; Chen, L.; Li, F.; Zhao, H.; Wang, X.; Zhou, G. Microstructure and texture evolution of a dynamic compressed medium-entropy CoCr_{0.4}NiSi_{0.3} alloy. *Crystals* **2023**, *13*, 1390. [[CrossRef](#)]
56. Hua, D.; Xia, Q.; Wang, W.; Zhou, Q.; Li, S.; Qian, D.; Shi, J.; Wang, H. Atomistic insights into the deformation mechanism of a CoCrNi medium entropy alloy under nanoindentation. *Int. J. Plast.* **2021**, *142*, 102997. [[CrossRef](#)]

Disclaimer/Publisher’s Note: The statements, opinions and data contained in all publications are solely those of the individual author(s) and contributor(s) and not of MDPI and/or the editor(s). MDPI and/or the editor(s) disclaim responsibility for any injury to people or property resulting from any ideas, methods, instructions or products referred to in the content.